Cellular chirality arising from the self-organization of the actin cytoskeleton

Yee Han Tee[1,7], Tom Shemesh[2,7,8], Visalatchi Thiagarajan[1], Rizal Fajar Hariadi[3], Karen L. Anderson[4], Christopher Page[4], Niels Volkmann[4], Dorit Hanein[4], Sivaraj Sivaramakrishnan[3], Michael M. Kozlov[5] and Alexander D. Bershadsky[1,6,8]

Cellular mechanisms underlying the development of left–right asymmetry in tissues and embryos remain obscure. Here, the development of a chiral pattern of actomyosin was revealed by studying actin cytoskeleton self-organization in cells with isotropic circular shape. A radially symmetrical system of actin bundles consisting of α-actinin-enriched radial fibres (RFs) and myosin-IIA-enriched transverse fibres (TFs) evolved spontaneously into the chiral system as a result of the unidirectional tilting of all RFs, which was accompanied by a tangential shift in the retrograde movement of TFs. We showed that myosin-IIA-dependent contractile stresses within TFs drive their movement along RFs, which grow centripetally in a formin-dependent fashion. The handedness of the chiral pattern was shown to be regulated by α-actinin-1. Computational modelling demonstrated that the dynamics of the RF–TF system can explain the pattern transition from radial to chiral. Thus, actin cytoskeleton self-organization provides built-in machinery that potentially allows cells to develop left–right asymmetry.

Processes that establish left–right asymmetry are among the most intriguing biological phenomena. Even though the mechanisms of establishment of left–right asymmetry in embryonic development are complex and involve the coordinated activity of many cells[1–3], the ability of cells to distinguish between left and right is evident in relatively simple systems, such as the collective movement of identical cells cultured on ring-shaped or stripe-shaped micropatterns[4–6], or in individual cells grown in isotropic conditions. Examples include neutrophil-like cells[7], some types of nerve cell[8,9], spreading platelets[10] and zebrafish melanophores[11].

Helical cytoskeletal polymers, such as actin filaments and microtubules, are natural candidates for initiating cellular left–right asymmetry as they are characterized by both longitudinal polarity and handedness[12,13]. Indeed, the left–right asymmetry in neutrophil polarization seems to depend on microtubules[7], whereas the chiral movement of cells on micropatterns[5,6] and the nuclear rotation in pigment cells[11] are mediated by the actin cytoskeleton. However, the specific cytoskeletal mechanisms leading to the establishment of a cellular asymmetry have yet to be deciphered. Understanding

how the intrinsic asymmetry of individual actin filaments can be translated into asymmetric behaviour of the entire actin cytoskeleton, and consequently of the entire cell, requires an exploration of actin cytoskeleton self-organization.

In cultured fibroblasts, spreading and polarization are accompanied by self-organization of the array of actin filament bundles (known also as actin cables, actin fibres or stress fibres)[14–17]. A closer look at the actin cytoskeleton revealed several classes of actin filament bundles that differ in protein composition, dynamics and mode of development[15,16,18–21]. In well-spread, elongated, but weakly motile cells, the predominant type of bundle is the 'ventral' stress fibre. These are anchored at each end to focal adhesions and are characterized by a striated morphology with alternating bands of α-actinin and myosin II (refs 16,17,19). Motile and spreading cells often form 'dorsal' fibres that grow from the focal adhesion towards the cell centre, presumably in a formin-dependent manner[19,22]. These fibres are enriched in α-actinin, palladin and VASP, and are largely devoid of myosin[19,23–25]. In addition, TFs, or arcs, are formed at the boundary between the lamellipodium and lamellum[18,26–28]. These fibres are characterized by the presence of
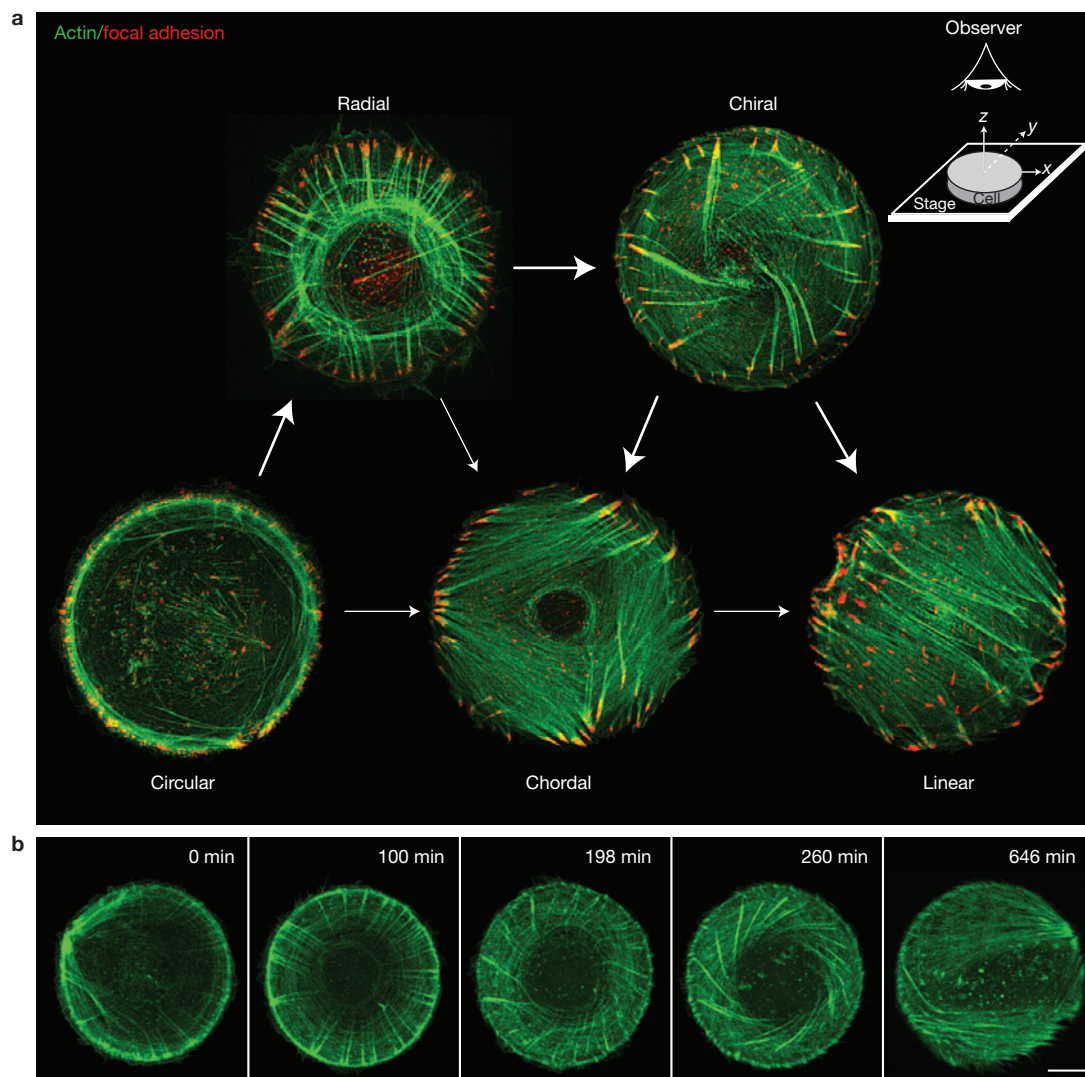
Figure 1 Distinct patterns of actin cytoskeleton self-organization. (**a**) A flow diagram of actin cytoskeleton transformations in cells plated on circular fibronectin islands of area 1,800 μm². Actin and focal adhesions were visualized with either co-transfection of LifeAct–GFP and mCherry–paxillin, or labelled with phalloidin and anti-paxillin antibodies. Maximum-projection images of actin, as viewed from above (see schematic diagram in top right corner), are shown. Actin cytoskeleton self-organizes into five characteristic patterns—circular, radial, chiral, chordal and linear. The flow diagram is derived from live observations of actin dynamics in 59 cells pooled from five experiments. Thick arrows show prevalent transitions. Thin arrows show rarely observed transitions (2–3 observations). (**b**) A typical example of the dynamic self-organization of the actin cytoskeleton. The actin cytoskeleton first organized into the radial pattern (100 min). The RFs began to tilt (198 min), leading to the chiral pattern organization (260 min). The actin cytoskeleton can break the chiral symmetry by self-organizing into the linear array (646 min). The actin cytoskeleton was visualized by transfection with LifeAct–GFP. Full-length sequence is shown in Supplementary Video 1. Scale bar, 10 μm.

tropomyosin 4 and myosin IIA (refs 23,27,28), and move from the cell periphery in a centripetal direction.

It seems that the system of actin fibres is dynamically richer than one would expect. By studying cells confined to circular adhesive islands, we demonstrate that dynamic actin fibres associated with focal adhesions can generate a chiral pattern with uniform handedness. The handedness of the chiral pattern was shown to be regulated by the actin crosslinking protein α-actinin. We studied in detail the dynamics of the actin fibres and the mode of their interaction and proposed a physical model accounting for the observed phenomena. Thus, our results suggest a basic cytoskeletal mechanism for the establishment of left–right asymmetry in cells.

RESULTS

Types of pattern formed by the actin cytoskeleton in cells plated on circular adhesive islands

To dissect the process of actin cytoskeleton self-organization from cell shape change, we studied cell behaviour using circular adhesive islands. Analysis of 100 videos, recorded over a period of up to 12 h, revealed the formation of several distinct arrays. These were characterized by the actin structures from which they were composed, as well as the typical transitions observed between them (Fig. 1a and Supplementary Videos 1 and 2).

At the early stages of actin network self-organization, a circumferential actin bundle underlying the circular cell boundary
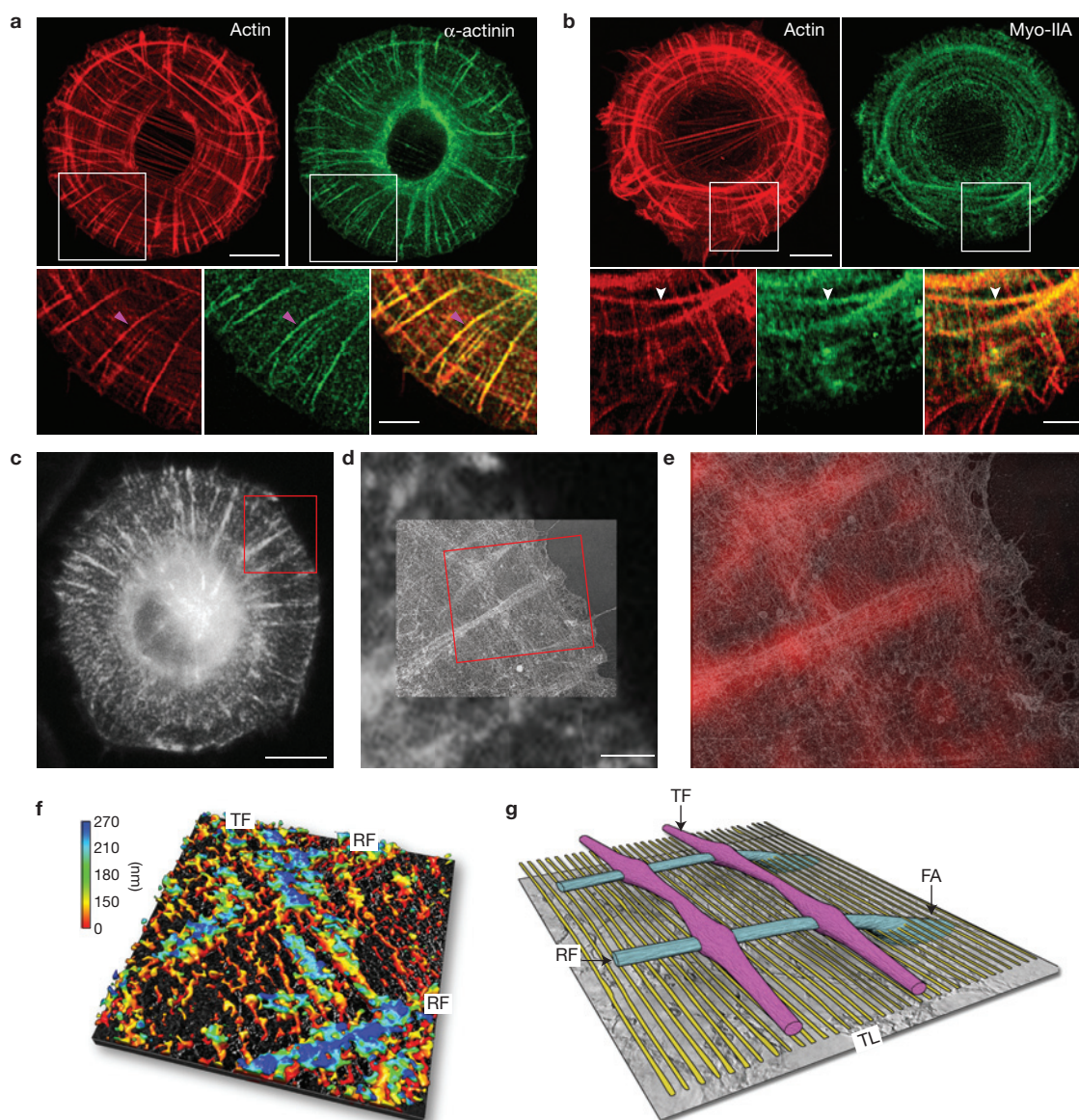
Figure 2 Composition and structure of RFs and TFs. (**a,b**) Actin was visualized by TRITC–phalloidin staining, α-actinin-1 by transfection with GFP–α-actinin-1 (**a**) and myosin IIA by anti-myosin-IIA antibody staining (**b**). Small panels are the enlarged images of the outlined regions and their superimpositions. α-actinin-1 marks RFs (magenta arrowheads) and myosin IIA marks TFs (white arrowheads) respectively. Scale bars, 10 μm; 4 μm (small panels). (**c–g**) Correlative light and electron microscopy of RFs and TFs. (**c–e**) Cells were plated on micropatterned fibronectin islands on an electron-microscopy-amenable substrate. The red rectangle in **c** marks the region shown in **d**. RFs and TFs were visualized by transfection of GFP–α-actinin-1 in **c,d** and the actin marker tdTomato–F-tractin in **e**. (**d,e**) Overlays of the corresponding electron microscopy image on the fluorescence image. Scale bars, 10 μm (**c**); 2 μm (**d**). (**e**) An enlarged view of the red-outlined region in **d** showing the correlation between the actin fluorescence (red) and electron microscopy image (protein material white) of the fibres. (**f**) A surface representation of a three-dimensional tomographic reconstruction of the region in **d,e**. The heights of the features are mapped to the colour key (in nanometres). TFs are found at the same height as the RFs (primarily blue and cyan). A thin transverse layer of actin filaments is visible as red/yellow striations (see also tomogram sections in Supplementary Fig. 2 and Supplementary Video 4). (**g**) Schematic model of morphological features. Two RFs (blue) are depicted attaching to the membrane–ECM interface (grey) at putative focal adhesions (FA) near the cell edge. Two TFs (pink) are also depicted crossing the RFs. TL (yellow)—a layer of transversally oriented thin filaments. Another thin, isotropic and sparse actin network layer can also be observed beneath these features near the membrane–ECM interface (see also Supplementary Fig. 2).

was formed along with peripheral focal adhesions (Fig. 1a). In most cases (70% of the videos observed), this 'circular pattern' transformed into a 'radial pattern' that was characterized by the appearance of straight actin fibres (about 20 per cell), growing radially towards the cell centre from peripheral focal adhesions (Fig. 1a and Supplementary Video 1). Concomitantly, numerous TFs emerged at the cell periphery parallel to the cell edge and moved centripetally (Supplementary Video 1).

Subsequently, in about 80% of cells, the RFs uniformly tilt in the same direction forming the 'chiral pattern' (Fig. 1a and Supplementary Videos 1 and 2). The TFs, while moving centripetally, continue to bridge the RFs. Thus, owing to tilting of the RFs, the velocity of
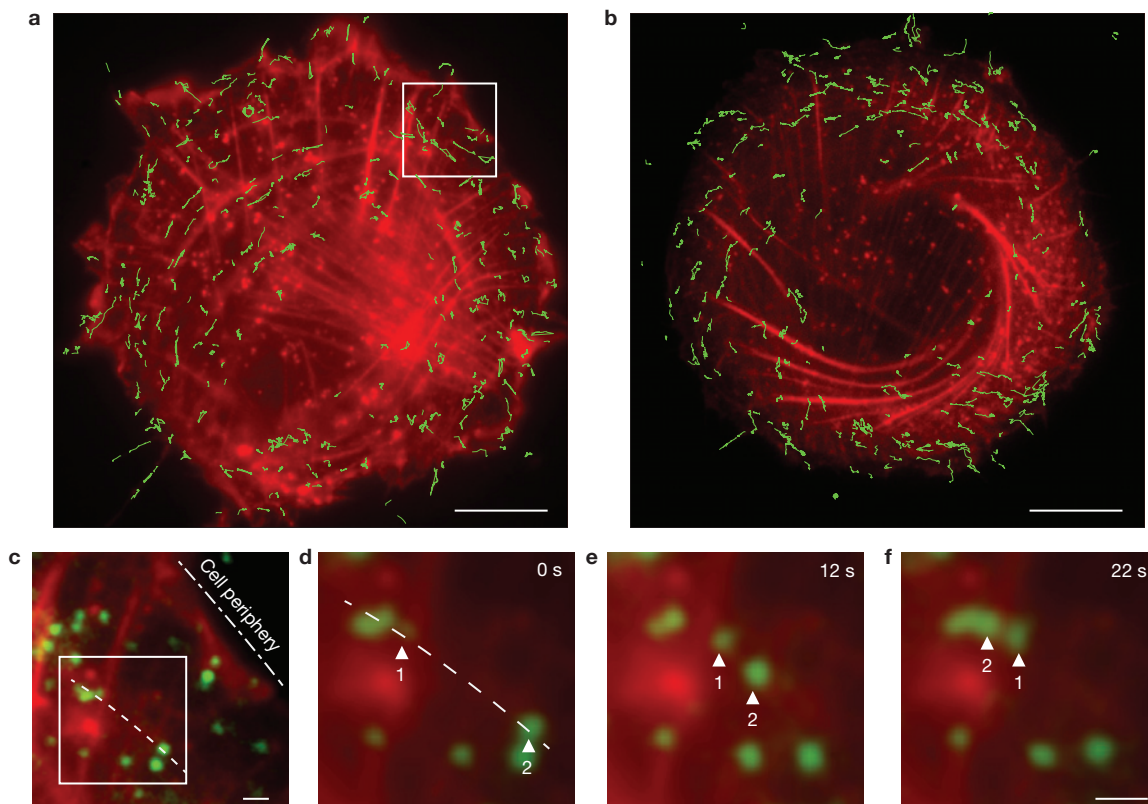
Figure 3 Probing of actin fibres in permeabilized cells with myosin-V-coated nanoparticles. (**a,b**) Movement trajectories (green) of fluorescent nanoparticles coated with myosin V along the actin cytoskeleton (red) in fixed extracted cells with radial (**a**) and chiral (**b**) patterns. Almost all trajectories go along TFs; movement along RFs is limited. The white square in **a** marks the view shown in **c**. Scale bars, 10 μm. (**c–f**) A high-magnification view of myosin V nanoparticle movement along a single TF. (**c**) A view of the actin cytoskeleton (red) after extraction. White-outlined region: the TF decorated with myosin V nanoparticles (green) is marked by a dashed line. (**d–f**) Sequential images from the live imaging of myosin V nanoparticles moving along the TF. Nanoparticles 1 and 2 (white arrowheads) move in opposite directions along the TF. Scale bars, 1 μm. The full-length sequence is shown in Supplementary Video 6.

the TFs, in addition to the radial component, acquires a tangential component. As a result, the motion of the TFs becomes reminiscent of the movement of a liquid element in swirling flow (Supplementary Videos 1 and 2).

The chiral swirling stage continued for several hours and was succeeded by either 'chordal' or 'linear' patterns. At the chordal stage, several families of straight, parallel actin fibres were formed in a chord-like fashion near the cell edge (Fig. 1a). The linear, seemingly ultimate, pattern is characterized by a single array of parallel actin fibres spanning the entire cell (Fig. 1a). Actin fibres comprising the chordal and linear patterns were associated with peripheral focal adhesions at both ends, resembling the 'ventral' stress fibres[16,17] in cells polarized under unconstrained conditions. A typical example of actin evolution is depicted in Fig. 1b (see also Supplementary Video 1).

Molecular composition and organization of RFs and TFs

Characterization of actin fibres revealed that RFs were enriched in the actin-crosslinking protein α-actinin-1 (ref. 29; Fig. 2a), as well as zyxin and VASP (Supplementary Fig. 1a,c), but were largely depleted of myosin II (Fig. 2b), thus resembling 'dorsal' stress fibres[19]. In contrast, the TFs contained significantly lower levels of α-actinin-1

(Fig. 2a) but were enriched with myosin IIA (Fig. 2b), thus resembling 'transverse arcs'[19,23,27].

TFs crossed RFs at each focal plane in a confocal microscopy Z-section of the cell edge (Supplementary Video 3). This suggests that these two families of actin fibres can physically interact. Three-dimensional reconstruction of electron tomography revealed prominent fibres extending radially from the cell edge (Fig. 2c–e), along with TFs located above the substrate at the same height as the RFs (150–250 nm; Fig. 2f and Supplementary Fig. 2 and Supplementary Video 4). A cross-sectional view of the RFs and TFs showed how the two interact (Supplementary Fig. 2e). An additional, sheet-like actin network consisting of thin actin bundles oriented parallel to the cell edge was also present at a height of ~100 nm (Fig. 2f,g and Supplementary Fig. 2b,e,f).

To further characterize RFs and TFs, we probed Triton-X-100-permeabilized and fixed cells with fluorescent DNA origami nanoparticles conjugated with myosin V or VI molecules in an ATP-containing 'motility buffer'[30]. We confirmed that the myosin-V- and -VI-coated nanoparticles could serve as faithful probes to assess actin filament polarity by observing their movement in opposite directions along filopodia, which contain actin bundles with well-defined polarity[31] (Supplementary Video 5). We subsequently showed that
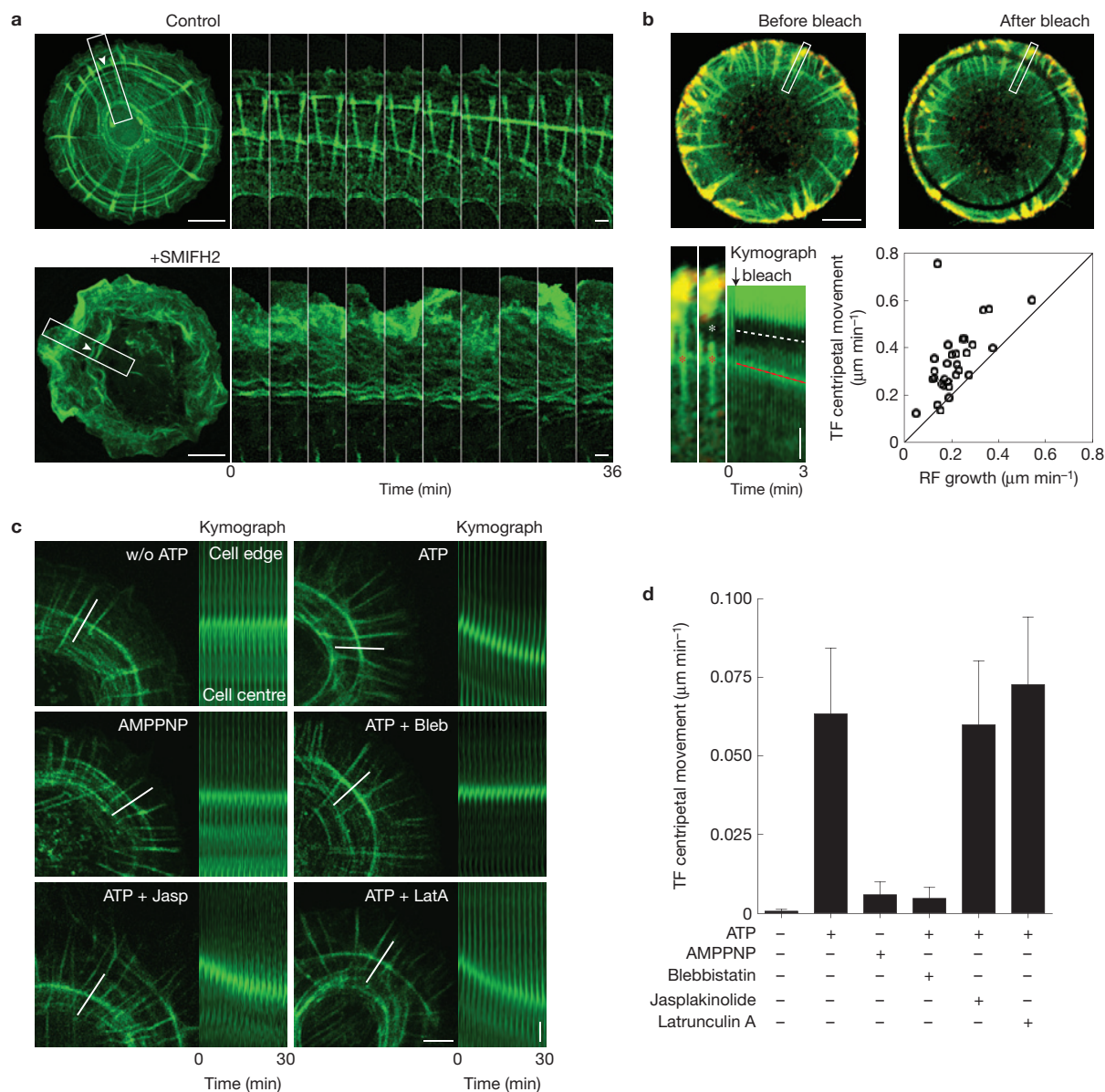
Figure 4 Dynamics of RFs and TFs. (**a**) The formin inhibitor SMIFH2 interferes with the formation of RFs. Images of an untreated control and 10 μM SMIFH2-treated cells and their sequential high-magnification views (white-outlined region) of the RFs and TFs. Scale bars, 10 μm; 2 μm (high magnification). See also Supplementary Video 7. (**b**) Image of a cell transfected with GFP–actin and mCherry–paxillin before and after a ring region was photobleached. Enlarged white-outlined region shows a photo-marked RF (white asterisk) associated with focal adhesion and a neighbouring TF (red asterisk). The kymograph shows the centripetal movement of the bleached zone (white dashed line) and TF (red dashed line); corresponding velocities are plotted in the graph. $n = 30$ pairs of fibres from 16 cells pooled from three independent experiments. Diagonal of the graph corresponds to equal velocities of TF movement and RF growth. RF growth rate ($0.21 \pm 0.09\,\mu m\,min^{-1}$) was lower than TF centripetal movement ($0.35 \pm 0.14\,\mu m\,min^{-1}$; mean $\pm$ s.d., $P < 0.0001$ by two-tailed unpaired Student's t-test). Scale bar, 10 μm. Vertical scale bar, 2 μm. (**c**) ATP- and myosin-dependent movement of TFs in permeabilized cells. Actin was labelled with AlexaFluor-488–phalloidin. Kymographs, taken along the white lines indicated in each image, are shown for each experimental condition. Concentrations of reagents used: 2 mM ATP, 2 mM AMPPNP, 100 μM blebbistatin (Bleb), 1 μM jasplakinolide (Jasp) and 1 μM latrunculin A (LatA). Scale bar, 5 μm. Vertical scale bar, 1 μm. (**d**) Graph showing the velocities of TF centripetal movement in each condition. Bars represent mean $\pm$ s.d. $n = 30$ TFs pooled from 6–10 cells for each experimental condition. The experiments were repeated 3 times for each condition. The average velocity of ATP-induced centripetal movement of TF in permeabilized cells is approximately fivefold slower than the movement of TF in living cells. The difference in velocities is statistically significant ($P < 0.001$) between without (w/o) ATP and ATP, ATP and AMPPNP, ATP and ATP + Bleb; nonsignificant between ATP and ATP + Jasp or ATP and ATP + LatA by one-way analysis of variance (ANOVA) with Bonferroni *post hoc* correction.

in cells at radial and chiral stages, both nanoparticle types travelled along TFs, but not RFs (Fig. 3a,b and Supplementary Fig. 3a). The nanoparticles were occasionally found attached to the RFs; however,

these rarely demonstrated any directional movement. The movement of both myosin-V- and myosin-VI-coated nanoparticles along the TFs could proceed in either direction, which strongly suggests that

TFs contain actin filaments with opposite polarity (Fig. 3c–f and Supplementary Fig. 3b–e and Supplementary Video 6).

Formin-dependent growth of RFs and myosin-II-dependent movement of TFs

To elucidate the role of formin- and Arp2/3-driven actin polymerization in cytoskeletal reorganization, we used small-molecule inhibitors, SMIFH2 (ref. 32) and CK666 (ref. 33), respectively. Formin inhibition blocked RF formation; TFs continued to form but their centripetal movement was hindered (Fig. 4a and Supplementary Video 7). Washing out the inhibitor restored both the growth of the RFs, and the centripetal movement of the TFs (Supplementary Video 8). Inhibition of Arp2/3 led to the disappearance of both RFs and TFs and enhanced the formation of filopodia-like structures (Fig. 5), in agreement with Arp2/3 knockdown experiments[34,35].

To study the relative movement of the RFs and TFs, cells were labelled with GFP–actin and the RFs were photo-marked by photobleaching a narrow circular band close to the cell periphery (Fig. 4b). By observing centripetal translocation of the bleached zone away from the focal adhesion, we demonstrated and measured the growth of RFs. The centripetal movement of an adjacent interacting TF was simultaneously monitored. Comparison of these two velocities revealed that the instantaneous centripetal velocity of an individual TF was consistently higher than the local growth rate of RFs in its immediate proximity (Fig. 4b).

The centripetal movement of TFs can be reproduced in Triton-X-100-permeabilized cells following the addition of ATP (Fig. 4c). AMPPNP, a non-hydrolysable analogue of ATP, did not induce movement of TFs (Fig. 4c,d). The ATP-driven movement of TFs in permeabilized cells was blocked by blebbistatin (Fig. 4c,d), which inhibits myosin II (ref. 36). Actin dynamics was not involved in the ATP-driven retrograde movement of TFs because the movement velocity was not affected by either the F-actin stabilizer jasplakinolide or the actin polymerization inhibitor latrunculin A (Fig. 4c,d).

Together, these results suggest that the centripetal motion of TFs in cells is a superposition of two distinct movements: a motion that results from RF growth, which is driven by formin-dependent actin polymerization, and a centripetal motion relative to the RFs, which is driven by myosin-IIA-dependent contractility of the TFs.

Myosin-II-driven contractility was critically important, not only for the centripetal motion of the TFs, but for the assembly and integrity of the entire TF–RF system. Suppressing myosin-II activity by blebbistatin or the Rho-kinase inhibitor Y-27632 (ref. 37) completely abolished actin self-organization (Fig. 5 and Supplementary Video 9).

Unlike actin polymerization and contractility inhibitors, total disruption of microtubules by nocodazole did not affect the sequence of events during actin pattern formation, including the transition from radial-to-chiral stage (Fig. 5 and Supplementary Fig. 4 and Supplementary Video 10).

Left–right asymmetry of the chiral pattern and its reversal by α-actinin-1

The chiral pattern is characterized by left–right asymmetry. An assessment of swirling direction by live imaging of more than a hundred cells revealed that swirling always occurs in an anticlockwise (ACW) direction as in Fig. 1. Disruption of microtubules did not affect the
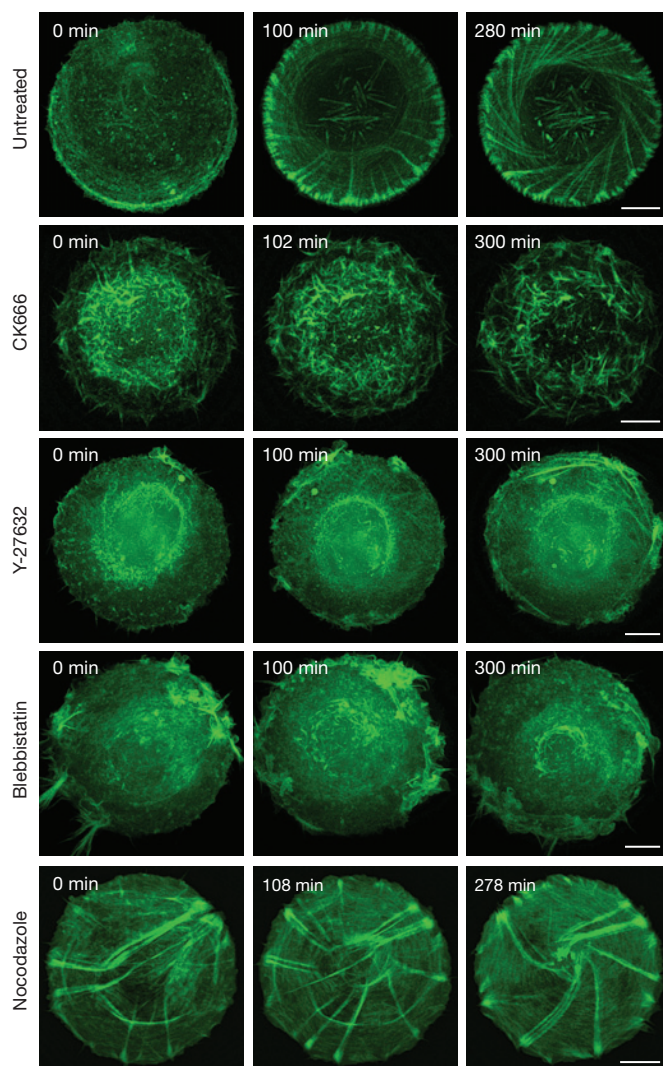

Figure 5 The influence of Arp2/3-mediated actin polymerization, actomyosin contractility and microtubule integrity on the evolution of actin organization. Selected image sequences from the live imaging of actin dynamics in cells transfected with either LifeAct–GFP or tdTomato–F-tractin (pseudo-coloured green). Cells were treated with 100 μM of the Arp2/3 inhibitor CK666, 30 μM of the Rho-kinase inhibitor Y-27632, 50 μM of the myosin II inhibitor blebbistatin, or 1 μM of the microtubule inhibitor nocodazole. Untreated control cells progressed from the radial (100 min) to chiral (280 min) stage. Treatment with the Arp2/3 inhibitor abolished the formation of the actin fibres and enhanced the formation of filopodia-like structures. Inhibitors of myosin-II-driven contractility (Y-27632 and blebbistatin) completely abolished formation of the actin fibre system. Microtubule disruption with nocodazole did not interfere with the process of actin self-organization. Scale bars, 10 μm. A full-length sequence of an untreated control cell is provided as Supplementary Video 2. Full-length sequences of both Y-27632-treated and blebbistatin-treated cells are provided as Supplementary Video 9. A full-length sequence of a nocodazole-treated cell is provided as Supplementary Video 10. See also images of nocodazole-treated cells in Supplementary Fig. 4.

swirling direction ($n = 47$ videos of nocodazole-treated cells were assessed; Fig. 5 and Supplementary Fig. 4 and Supplementary Video 10).

Surprisingly, several cases of clockwise (CW) swirling were observed in cells expressing labelled α-actinin-1 alone or together with actin markers (Fig. 6a and Supplementary Video 11). Unlike
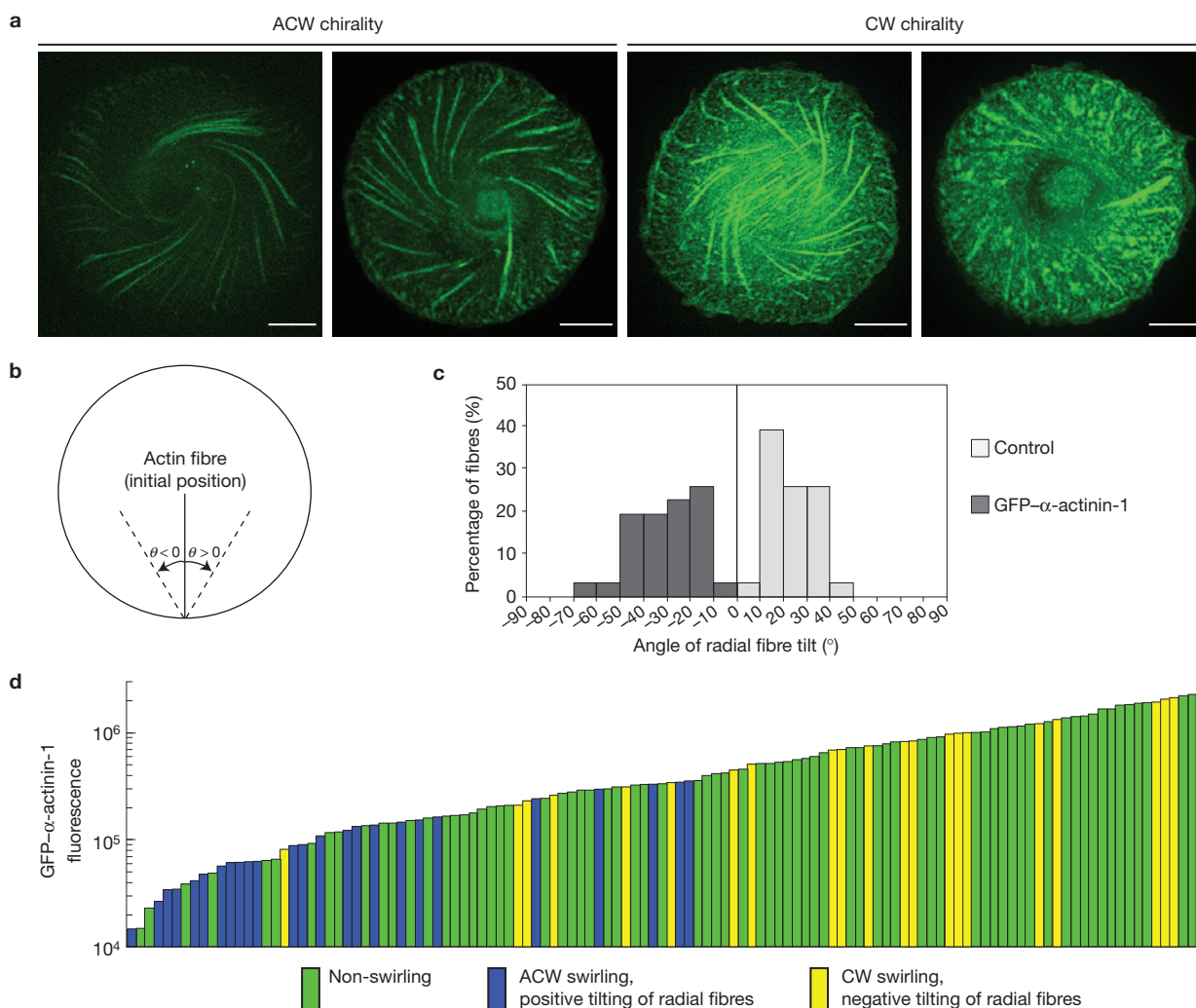
Figure 6 The effect of α-actinin-1 overexpression on the frequency and handedness of the chiral swirling. (**a**) Differential GFP–α-actinin-1 expression can regulate the direction of chirality. Cells expressing lower or higher levels of GFP–α-actinin-1 demonstrated ACW and CW swirling respectively. Scale bars, 10 μm. See also Supplementary Video 11. (**b**) The angle of actin fibre tilt was defined as either positive or negative, on the basis of the deviation from its initial position. Arrows indicate direction of tilt. Dashed lines represent positions of actin fibre after tilting. (**c**) Histogram showing the distribution of radial actin fibre tilt angles (°) in a control cell and a cell overexpressing GFP–α-actinin-1. Note that RFs in cell overexpressing GFP–α-actinin-1 tilt in the opposite direction as compared with control cell. Thirty actin fibres of a representative cell were analysed for each cell type. (**d**) GFP–α-actinin-1 expressing cells were filmed to follow the dynamics of actin cytoskeleton self-organization. α-actinin-1 expression level was assessed by measuring the total GFP fluorescence intensity for each cell. The *y* axis represents fluorescence intensity in a log scale; the cells were sorted by ascending order of their α-actinin-1 expression level along the *x* axis. Each bar on the histogram represents an individual cell. Colour-coding indicates the type of actin cytoskeleton dynamics for each cell. Green—cells that do not demonstrate swirling during the entire period of observation (∼10 h). Blue—cells demonstrating positive tilt of RFs and ACW swirling similar to a control cell. Yellow—cells demonstrating negative tilt of RFs and CW swirling. One hundred and twenty cells were pooled from two independent experiments. The average level of α-actinin-1–GFP intensity in cells exhibiting CW chirality (22 cells) was sevenfold higher than in cells exhibiting ACW chirality (25 cells; *P* < 0.0001 by two-tailed unpaired Student's *t*-test with Welch's correction).

α-actinin-1, the expression of α-actinin-binding protein, zyxin or the zyxin partner[38] VASP did not change the swirling direction (Supplementary Fig. 1b,d).

To quantify the effect of α-actinin-1 expression on the establishment of chirality, we measured the total GFP fluorescence, and hence expression level, of GFP–α-actinin-1 in 120 individual cells (Fig. 6d). In the cells with a low expression of GFP–α-actinin-1, the radial-to-chiral transition was manifested by positive tilting of RFs, giving rise to an ACW swirling, similarly to that in control cells (Fig. 6b,c). With increasing α-actinin-1 expression, the fraction of

cells bypassing the swirling stage increased (Fig. 6d). When cells that had a high expression of α-actinin-1 proceeded into the chiral stage, the RFs tilted in a negative direction, giving rise to CW swirling (Fig. 6a–d and Supplementary Video 11).

α-actinin-1 forms antiparallel homodimers that crosslink actin filaments[39]. It also plays a role in focal adhesion assembly[40,41]. To elucidate the function of α-actinin-1 in the radial-to-chiral transition, we examined α-actinin-1 mutants and α-actinin-1 knockdown cells. The truncated α-actinin-1 mutant GFP–ABDdel-α-actinin-1 lacks the actin-binding domain[41] and cannot crosslink actin filaments[29]
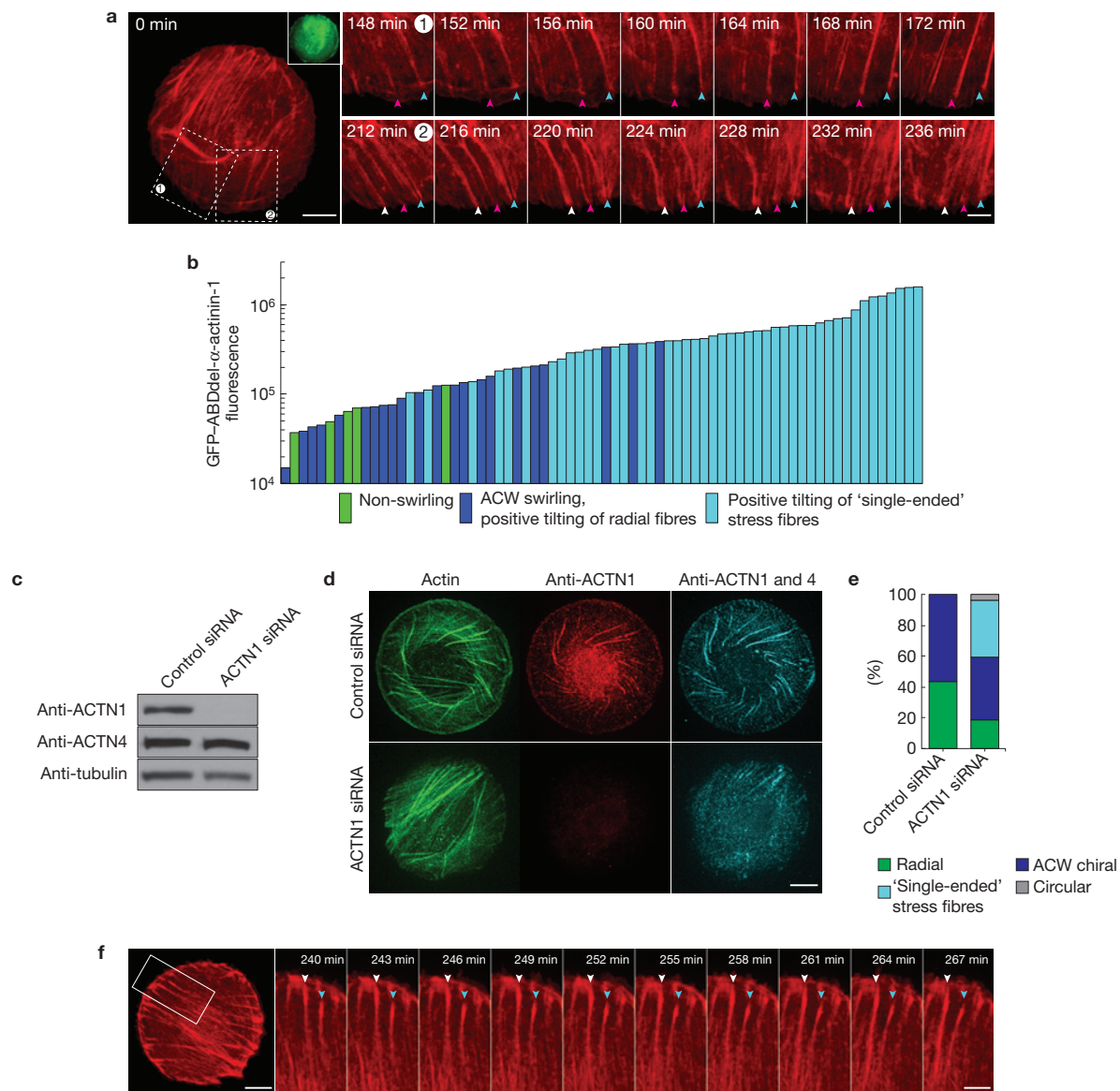
Figure 7 The effects of α-actinin-1 dominant-negative mutant and knockdown. (**a**) Typical view of the actin (tdTomato–F-tractin) organization in cells overexpressing GFP–ABDdel-α-actinin-1 (inset). Sequential images from regions 1 and 2 (outlined with dashed lines) show 'single-ended' stress fibres (coloured arrowheads) tilting in a positive direction. Scale bars, 10 μm; 5 μm (high magnification). See also Supplementary Fig. 5 and Supplementary Video 12. (**b**) Cells expressing GFP–ABDdel-α-actinin-1 and co-transfected with the actin marker (tdTomato–F-tractin) were filmed to follow their actin cytoskeleton dynamics. ABDdel-α-actinin-1 expression was assessed by measuring the total GFP fluorescence intensity for each cell. As in Fig. 6d the cells were sorted by ascending order of GFP–ABDdel-α-actinin-1 expression. Colour-coding of the histogram indicates the type of actin dynamics for each cell. Blue and green denote, as in Fig. 6d, ACW swirling or non-swirling cells respectively. Cyan—cells forming long 'single-ended' stress fibres tilting in the positive direction as shown in **a**. Seventy-two cells were pooled from two independent experiments. (**c**) Western blot showing α-actinin-1 (ACTN1) and α-actinin-4 (ACTN4) levels in cells treated with scramble (control) or anti-ACTN1 siRNA; α-tubulin was used as a loading control. Uncropped scan is shown in Supplementary Fig. 9. (**d**) Actin and α-actinin in control and ACTN1-siRNA-treated cells 5 h after spreading. Cells were immunolabelled using an antibody against ACTN1-only and an antibody against both ACTN1 and ACTN4, as well as with phalloidin to visualize actin. Scale bar, 10 μm. ACTN1-siRNA-affected cells developed long stress fibres and no RFs. (**e**) The percentage of control or ACTN1 siRNA-treated cells demonstrating various patterns of actin organization—radial (green), ACW chiral (blue), circular (grey) and a system of long stress fibres (cyan). Thirty control cells and 60 ACTN1 siRNA cells were assessed from a representative experiment. Three independent experiments were performed. (**f**) Long stress fibres in ACTN1-siRNA-treated cells demonstrated unidirectional positive tilting like 'single-ended' stress-fibres in cell expressing GFP–ABDdel-α-actinin-1. The sequence shows the actin dynamics (tdTomato–F-tractin) within the cell region marked by the white rectangle. Two 'single-ended' stress fibres are marked by coloured arrowheads. Scale bars, 10 μm; 5 μm (high magnification). See also Supplementary Video 13.

(Supplementary Fig. 5a). Moreover, such truncated α-actinin can heterodimerize with endogenous α-actinin[42], thereby acting as a dominant negative mutant perturbing α-actinin-1-mediated actin

filament crosslinking. Expression of GFP–ABDdel-α-actinin-1 abolished RF formation, but resulted in the formation of a different type of long actin fibres (termed 'single-ended' stress fibres), which

contained myosin IIA but, unlike regular stress fibres, were usually anchored to a single focal adhesion (Fig. 7a and Supplementary Fig. 5b). Time-lapse imaging revealed that the single-ended stress fibres were dynamic and tilted over time (Fig. 7a and Supplementary Video 12). The direction of tilting was positive (Supplementary Fig. 5c), similar to RFs in control cells, and hence the cells preserved ACW chirality. Cells expressing a high level of another α-actinin-1 mutant, SR12–GFP (ref. 41; Supplementary Fig. 5a), either failed to progress beyond the circular stage (Supplementary Fig. 6a), or like cells expressing GFP–ABDdel-α-actinin-1, formed single-ended stress fibres that tilted in a positive direction (Supplementary Fig. 6b).

α-actinin-1 silencing by short interfering RNA (ACTN1 siRNA) was specific for α-actinin-1 and did not reduce the level of α-actinin-4 (Fig. 7c,d). About 40% of ACTN1-siRNA-expressing cells demonstrated a pattern typical for cells expressing GFP–ABDdel-α-actinin-1 with numerous single-ended stress fibres, tilting in the positive direction, similar to RFs in control cells (Fig. 7e,f and Supplementary Video 13).

Together, these results show that the chiral pattern of actin cytoskeleton self-assembly has an intrinsic left–right asymmetry, which can be modulated by α-actinin-1. α-actinin-1 overexpression reduced the fraction of cells entering the chiral stage, suggesting that α-actinin-1 is not required for, but rather hinders, actin cytoskeleton swirling. Accordingly, the amount of non-swirling cells was systematically lower in cells expressing the ABDdel-α-actinin-1 mutant, as well as in α-actinin-1 knockdown cells (Fig. 7b,e). The cytoskeleton of cells with high levels of α-actinin-1 that underwent swirling did so in the opposite direction to that of both control cells, and cells with lower levels of exogenous α-actinin-1. Neither expression of α-actinin-1 mutants, nor depletion of α-actinin-1, changed swirling direction, suggesting that the crosslinking activity of α-actinin-1 is essential to switch the handedness of swirling.

This chiral swirling of the actin network directed the chiral motion of other cellular components. Rotation of the microtubule array occurred in the ACW direction together with actin swirling (Supplementary Video 14). Fibronectin-coated beads attached to the surface of cells at the chiral stage moved in an ACW fashion together with the bulk of actin (Supplementary Fig. 7). Thus, development of actin chirality leads to the development of chirality within the entire cell.

Computational modelling of the self-organization of actin fibres

We constructed a computational model for actin fibre self-organization, based on the physical properties of radial and transverse elements, and the specific interactions between actin fibres that are suggested by the experimental results. We simulate the time evolution of the system and determine its predicted dynamic patterns. For a detailed description of the model see Supplementary Note.

RFs are modelled as elastic rods that originate from focal adhesions and polymerize in a formin-dependent manner towards the cell centre. The polymerization kinetics are related to the mechanical stresses within the fibres as described by a model of formin-mediated polymerization of actin filaments[43,44]. In contrast to the RFs, TFs act as active contractile actomyosin elements and are therefore associated in our model with an inherent contractile stress. We reason that dynamic interactions between TFs and RFs allow alternate binding

and unbinding events so that the TFs are bound along the RFs, but may slide relative to them (Fig. 8a).

As RFs are radially oriented, the stress produced by the actomyosin machinery within TFs generates a centripetal force that moves TFs along RFs towards the cell centre. These contractile stresses within TFs are transmitted to the RFs through the TF–RF bonds, and result in forces with both a centripetal component that pull the RFs inward, and a tangential component that produces a rotational moment, acting to bend the RFs about their anchoring points at the focal adhesion.

Our simulations show that, starting from an initial circular stage, RFs elongate directly towards the cell centre and TFs move centripetally along them at a rate that is a combination of RF growth rate, and the rate of relative TF–RF motion (Fig. 8b and Supplementary Video 15). This corresponds to the radial pattern observed experimentally (see above, Fig. 1 and Supplementary Videos 1 and 2).

Following this radial stage, our model predicts a spontaneous loss of radial orientation of the RFs and their collective unidirectional tilting, resulting in a pattern approximating the observed chiral pattern (Fig. 1 and Supplementary Videos 1 and 2). The metastability of the radial pattern with respect to the transition into the chiral pattern is determined by the tendency of the TFs to contract, while maintaining their attachment to the RF. Consequently, deviation of a RF away from the radial orientation is followed by a redistribution of TFs that are bound to it from either side, resulting in a non-vanishing bending moment about the RF origin, acting to amplify and propagate the initial deviation (Fig. 8c).

The handedness of the chiral pattern of actin fibres may arise from a possible rotation of individual actin filaments within the RFs. Owing to the dynamic TF–RF binding, such rotations are transmitted to TFs, analogously to a 'rack and pinion' gear system, where the 'pinion' corresponds to a rotating radial filament and the 'rack' to a TF (Fig. 8d). In this scheme, the direction of the axial rotation of filaments within the RF generates a frictional force that promotes a CW or an ACW swirl pattern, depending on the direction of filament rotation.

The origin of individual filament rotation could be the interaction between formin cappers and the helical actin structure. The barbed ends of actin filaments in the RFs are assumed to be oriented towards the focal adhesions[17,45] and polymerize at the focal adhesion by formins[19,22], in agreement with formin inhibition experiments (Fig. 4a). Formin dimers act as 'processive caps' that permit and enhance the incorporation of new actin subunits into the growing filament[46,47]. When unconstrained, a formin capper tracks along the right-handed long-pitch actin helix in a 'stair-stepping' mode[48,49], resulting in a formin rotation of ∼−14° about the filament axis with the addition of each new monomer (Supplementary Video 16).

Conversely, if the formin dimer is immobilized at the focal adhesion, but the pointed end of the filament is free to rotate, the bulk of the polymerizing actin filament will rotate around its axis by +14° in the opposite direction (Supplementary Fig. 8a and Supplementary Video 17), as was observed experimentally[50]. Such rotations are therefore expected to produce a persistent force that favours ACW swirl patterns.

If the filament is crosslinked by α-actinin in addition to having formin immobilized at the barbed end, filament rotation will effectively be prohibited some distance away from the barbed end. The addition of new actin monomers would therefore result in
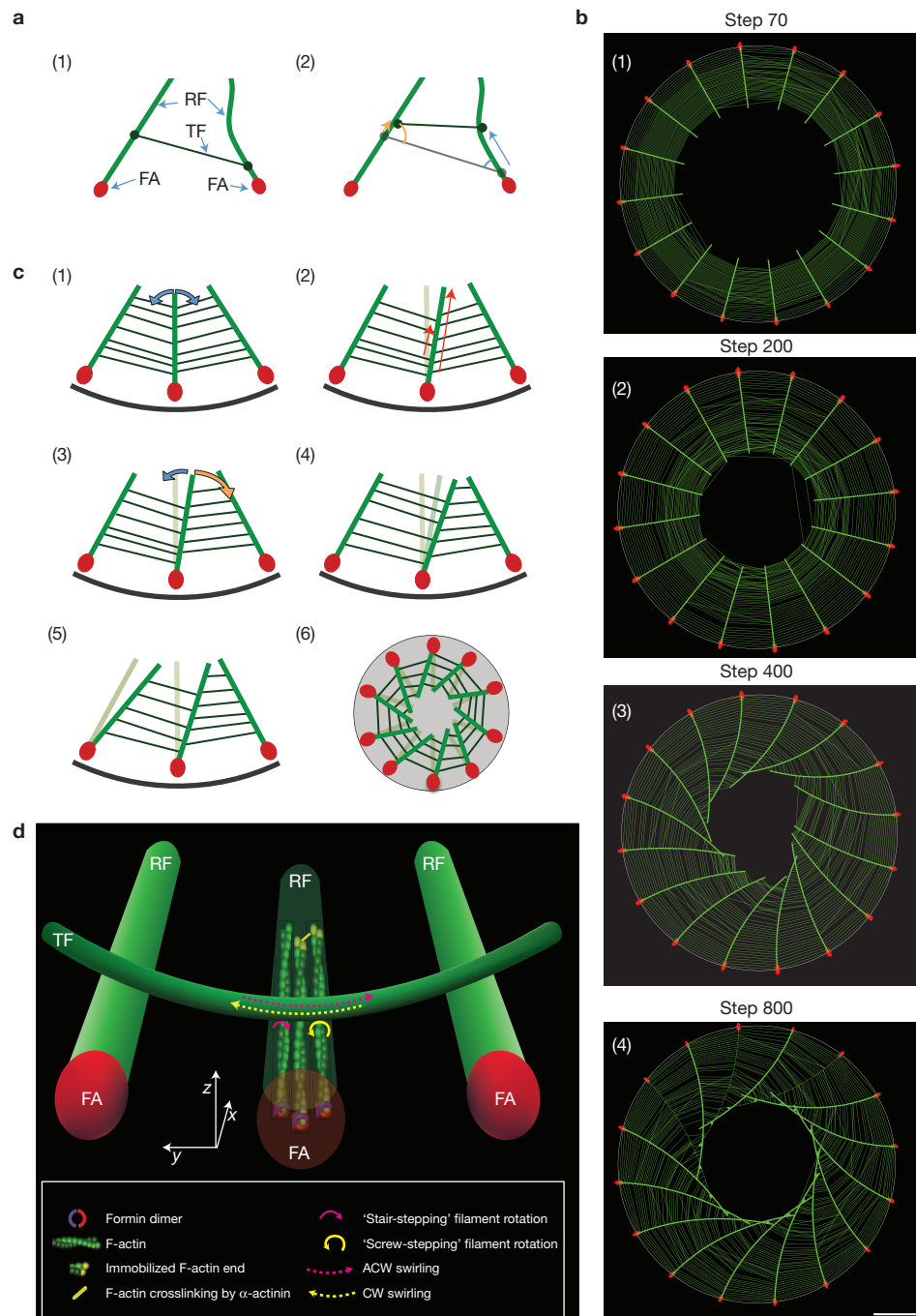
Figure 8 Physical model for the actin self-organization. (**a**) Schematic illustrating the forces driving the movement of TFs. (1) The ends of a TF (dark green) are bound to the sides of the RFs (light green). Focal adhesions (FAs) depicted in red. (2) Contractile forces within the TF drive the bound TF ends centripetally. Two successive positions of TF are depicted. The velocity of the bound ends (arrows) depends on the angle between the TF and the RF. (**b**) A simulation implementing the model shows the evolution of the actin system. Stimulation steps in arbitrary time units. (1–2) Global centripetal flow, comprising the radial growth of RFs (thick green lines) and centripetal motion of TFs (thin green lines). Focal adhesions indicated in red. (3) Slight inhomogeneity in TF distribution promotes deviation of RFs from the radial direction. (4) A stable swirling pattern is established. Scale bar, 10 μm. See Supplementary Video 15. (**c**) Schematic illustrating the instability of the radial configuration and emergence of the chiral pattern. (1) In the stable radial configuration of RFs (thick green line), the rotational torques (blue arrows) applied by the TFs (thin dark green line) are cancelled out. Focal adhesions depicted in red; black curve denotes the cell edge. (2) Slight deviation from the radial direction results in a faster redistribution of TFs along one side of the RF (red arrows designating redistribution velocities). (3) A net rotational torque is applied on RF (blue and orange arrows designating torque in each direction). (4) The torque rotates the RF in the direction of the initial deviation. (5) An imbalance of forces on the neighbouring RF, promoting radial deviations in the same direction. (6) The deviation propagates, resulting in a chiral pattern. (**d**) Individual actin filament rotation determines the direction of cytoskeleton swirling. An actin filament within the RFs can rotate in a positive angular direction (magenta arrow) under normal conditions or in a negative angular direction (yellow arrow) following α-actinin overexpression (see Supplementary Fig. 8). Friction between the rotating filament and the TF produces tangential forces (dotted arrows), promoting a preferred chirality direction of the swirl pattern.

the accumulation of torsional stress within the filament[49]. We have previously calculated that the stress in such filaments may be periodically relieved every ~12 stair-steps by a 'screw-step' motion, wherein the bulk of a filament rotates by −166° relative to the formin[49]. In this regime, the rotation velocity of a bound filament alternates between a slow rotation in one direction, and a fast rotation in the opposite angular direction (Supplementary Fig. 8b and Supplementary Video 18). The fast negative rotations are expected to dominate over the slow positive rotations (see Supplementary Note), and the net mean force produced by α-actinin bound filaments is expected to promote CW swirl patterns.

The relative abundance of filaments that are free to rotate versus those that are constrained by α-actinin in the system determines the average tangential force acting on the TF and, hence, the direction of the swirl pattern. At low α-actinin levels the net force is dominated by the freely rotating filaments, and ACW swirl patterns are promoted. As the expression of α-actinin increases, more filaments become immobilized. At a sufficiently high ratio of immobilized versus free filaments, CW swirl patterns become favourable (Fig. 8d). For a detailed derivation of these results, see Supplementary Note.

DISCUSSION

The goal of this work was to explore the patterns formed during actin fibre organization, under conditions that maintain a constant isotropic cell shape. This was done by plating fibroblasts onto circular adhesive islands. Under this condition, the actin cytoskeleton demonstrates characteristic patterns of self-organization, including a remarkable transition from a radially symmetric pattern, to a chiral pattern with a defined handedness. We investigated the dynamic behaviour of the main cytoskeletal components during this process and proposed a unifying model of chiral symmetry breaking during actin cytoskeleton self-organization.

The key elements of actin network self-organization are the RFs and TFs. Together these structures first form an isotropic radial pattern that undergoes a transition into the chiral pattern through a unidirectional tilting of RFs accompanied by a swirling motion of the TFs. The RFs, which grow from focal adhesions in a formin-dependent fashion, are enriched in α-actinin-1 and do not contain myosin II. These fibres resemble 'dorsal' stress fibres of migrating cells[15,19,22,24]. Experiments with myosin-V- and myosin-VI-coated nanoprobes showed that the myosin-binding sites of the actin filaments within the RFs are inaccessible to myosin heads. In contrast, the TFs, which resemble previously described 'transverse arcs'[15,18,19,23,27], are contractile elements because they are enriched in myosin IIA and contain actin filaments of opposite polarity as revealed by experiments with myosin-V- and -VI-coated nanoprobes.

We have demonstrated that the centripetal movement of TFs results from both RF polymerization and also translocation of TFs with respect to RFs. The existence of the former was demonstrated using a formin inhibitor to block the growth of RFs, as this restrained the centripetal motion of the TFs. The latter component of TF movement—myosin II-driven contraction—was demonstrated in permeabilized cells following the addition of ATP and in the absence of either actin polymerization or depolymerization. Accordingly, in intact cells, the velocity of TF translocation was shown to exceed the rate of RF growth. Our structural data demonstrated

that RFs and TFs physically interact with each other, forming an integrated system.

Notably, the polymerization of the RFs may depend on tension generated by TFs. This notion is substantiated by the fact that myosin II inhibition prevents the formation of both TFs and RFs. Indeed, as predicted theoretically[43] and supported in recent experimental studies[51,52], formin-driven actin polymerization is force-dependent.

To understand the physics behind radial pattern dynamics, and chiral pattern formation, we developed a computational model based on a proposed mechanism whereby TFs are translocated in a centripetal direction. This mechanism is based on a myosin-IIA-driven shortening of TFs and the dynamic binding–unbinding interactions between their ends and the sides of RFs. This essentially enables a TF to 'step' or 'walk' along RFs. The computation based on this model demonstrated a metastable character of the radial pattern and its spontaneous transformation into the chiral pattern.

The observed left–right asymmetry of the chiral pattern is explained in our model as a direct consequence of the polar and helical properties of the actin filament structure. We speculate that formin-driven rotation of polymerizing actin filaments demonstrated in vitro[50] also occurs for the coaligned actin filaments comprising the RF. This rotation can be transmitted to the TFs, and promotes ACW swirling as depicted in Fig. 8d.

The actin-crosslinking protein α-actinin-1 can modulate the handedness of the chiral pattern. Overexpression of α-actinin-1 hindered the transition from radial-to-chiral patterns; however, cells that did undergo such transitions demonstrated a swirling in the opposite direction to that in control cells. The crosslinking activities of α-actinin-1 seem to be critically important for the switch of chirality direction. Excessive crosslinking between actin filaments may inhibit their rotation further away from the formin cappers. Thus, torsional strain accumulates in the constrained filament with each addition of a new actin monomer. Relaxation of this strain may be achieved by a periodic rotation of the filament in the opposite direction to the rotation of an unconstrained filament[49]. Consequently, a CW swirling is promoted, as depicted in Fig. 8d. Thus, our hypothesis that the asymmetry of cytoskeleton swirling originates from the asymmetry of formin–actin interactions seems also to explain the reversal of swirling direction observed in α-actinin-1 overexpression experiments.

Irrespective of the specific mechanism, the existence of a distinct handedness in the chiral pattern, and its control by actin-associated proteins such as α-actinin-1, suggests that this phenomenon may be of a biological significance and one that is actively regulated by the cell. Similar 'swirl-like' images have also been observed during platelet spreading[10] and in cells under regular culture conditions[53], indicating that chiral actin organization can develop in unconfined cells.

Translation of the helical actin filament structure into the asymmetric left–right behaviour of the whole system could also be mediated by some myosins. Indeed, experimental and theoretical results suggest that myosins I, II and V can underlie the chiral behaviour of individual cells and cell collectives[9,54–58]. However, RFs that determine the swirling direction in our cells do not contain myosin and cannot bind it, suggesting that myosin does not contribute to the establishment of left–right asymmetry observed in this study. Finally, even though the centrosome and microtubule system seems to be a source of left–right asymmetry in the polarization of

neutrophil-like cells[7], disruption of microtubules in our cells does not prevent the development of a chiral actin pattern, nor change its handedness.

In conclusion, the main achievements of our study are the discovery of an intracellular actin organization mechanism that gives rise to a chiral pattern, and the proposal of a physical mechanism behind this phenomenon. This intrinsic cellular mechanism may play an important role in a variety of morphogenetic processes in single-cell and multicellular systems. The factors controlling the handedness of the chiral pattern await further experimental and theoretical exploration. □

METHODS

Methods and any associated references are available in the online version of the paper.

Note: Supplementary Information is available in the online version of the paper

AUTHOR CONTRIBUTIONS

A.D.B. conceived the study. Y.H.T., T.S., M.M.K. and A.D.B. designed the study, analysed the data and wrote the manuscript with input from all authors. Y.H.T. and V.T. performed most experiments. R.F.H. and S.S. performed the cytoskeletal probing with myosin-V- and -VI-coated nanoparticles and analysed the data. K.L.A., C.P., N.V. and D.H. performed the electron microscopy work comprising of correlative light and electron microscopy, electron tomography and tomographic three-dimensional reconstructions. T.S. and M.M.K. developed the computational model.

COMPETING FINANCIAL INTERESTS

The authors declare no competing financial interests.

1. Blum, M., Feistel, K., Thumberger, T. & Schweickert, A. The evolution and conservation of left–right patterning mechanisms. *Development* **141**, 1603–1613 (2014).
2. Coutelis, J. B., Gonzalez-Morales, N., Geminard, C. & Noselli, S. Diversity and convergence in the mechanisms establishing L/R asymmetry in metazoa. *EMBO Rep.* **15**, 926–937 (2014).
3. Yoshiba, S. & Hamada, H. Roles of cilia, fluid flow, and Ca²⁺ signaling in breaking of left–right symmetry. *Trends Genet.* **30**, 10–17 (2014).
4. Wan, L. Q. & Vunjak-Novakovic, G. Micropatterning chiral morphogenesis. *Commun. Integr. Biol.* **4**, 745–748 (2011).
5. Wan, L. Q. *et al.* Micropatterned mammalian cells exhibit phenotype-specific left–right asymmetry. *Proc. Natl Acad. Sci. USA* **108**, 12295–12300 (2011).
6. Chen, T. H. *et al.* Left–right symmetry breaking in tissue morphogenesis via cytoskeletal mechanics. *Circ. Res.* **110**, 551–559 (2012).
7. Xu, J. *et al.* Polarity reveals intrinsic cell chirality. *Proc. Natl Acad. Sci. USA* **104**, 9296–9300 (2007).
8. Heacock, A. M. & Agranoff, B. W. Clockwise growth of neurites from retinal explants. *Science* **198**, 64–66 (1977).
9. Tamada, A., Kawase, S., Murakami, F. & Kamiguchi, H. Autonomous right-screw rotation of growth cone filopodia drives neurite turning. *J. Cell Biol.* **188**, 429–441 (2010).
10. Hagmann, J. Pattern formation and handedness in the cytoskeleton of human platelets. *Proc. Natl Acad. Sci. USA* **90**, 3280–3283 (1993).
11. Yamanaka, H. & Kondo, S. Rotating pigment cells exhibit an intrinsic chirality. *Genes Cells* **20**, 29–35 (2015).
12. Henley, C. L. Possible origins of macroscopic left–right asymmetry in organisms. *J. Stat. Phys.* **148**, 741–775 (2012).
13. Vandenberg, L. N., Lemire, J. M. & Levin, M. It's never too early to get it Right: a conserved role for the cytoskeleton in left–right asymmetry. *Commun. Integr. Biol.* **6**, e27155 (2013).
14. Vasiliev, J. M. Spreading of non-transformed and transformed cells. *Biochim. Biophys. Acta* **780**, 21–65 (1985).
15. Small, J. V., Rottner, K., Kaverina, I. & Anderson, K. I. Assembling an actin cytoskeleton for cell attachment and movement. *Biochim. Biophys. Acta* **1404**, 271–281 (1998).
16. Tojkander, S., Gateva, G. & Lappalainen, P. Actin stress fibers–assembly, dynamics and biological roles. *J. Cell Sci.* **125**, 1855–1864 (2012).
17. Burridge, K. & Wittchen, E. S. The tension mounts: stress fibers as force-generating mechanotransducers. *J. Cell Biol.* **200**, 9–19 (2013).
18. Heath, J. P. Direct evidence for microfilament-mediated capping of surface receptors on crawling fibroblasts. *Nature* **302**, 532–534 (1983).
19. Hotulainen, P. & Lappalainen, P. Stress fibers are generated by two distinct actin assembly mechanisms in motile cells. *J. Cell Biol.* **173**, 383–394 (2006).
20. Naumanen, P., Lappalainen, P. & Hotulainen, P. Mechanisms of actin stress fibre assembly. *J. Microsc.* **231**, 446–454 (2008).
21. Vallenius, T. Actin stress fibre subtypes in mesenchymal-migrating cells. *Open Biol.* **3**, 130001 (2013).
22. Oakes, P. W., Beckham, Y., Stricker, J. & Gardel, M. L. Tension is required but not sufficient for focal adhesion maturation without a stress fiber template. *J. Cell Biol.* **196**, 363–374 (2012).
23. Tojkander, S. *et al.* A molecular pathway for myosin II recruitment to stress fibers. *Curr. Biol.* **21**, 539–550 (2011).
24. Kovac, B., Teo, J. L., Makela, T. P. & Vallenius, T. Assembly of non-contractile dorsal stress fibers requires α-actinin-1 and Rac1 in migrating and spreading cells. *J. Cell Sci.* **126**, 263–273 (2013).
25. Gateva, G., Tojkander, S., Koho, S., Carpen, O. & Lappalainen, P. Palladin promotes assembly of non-contractile dorsal stress fibers through VASP recruitment. *J. Cell Sci.* **127**, 1887–1898 (2014).
26. Shemesh, T., Verkhovsky, A. B., Svitkina, T. M., Bershadsky, A. D. & Kozlov, M. M. Role of focal adhesions and mechanical stresses in the formation and progression of the lamellipodium-lamellum interface. *Biophys. J.* **97**, 1254–1264 (2009); correction **97**, 2115 (2009).
27. Burnette, D. T. *et al.* A role for actin arcs in the leading-edge advance of migrating cells. *Nat. Cell Biol.* **13**, 371–381 (2011).
28. Burnette, D. T. *et al.* A contractile and counterbalancing adhesion system controls the 3D shape of crawling cells. *J. Cell Biol.* **205**, 83–96 (2014).
29. Sjöblom, B., Salmazo, A. & Djinović-Carugo, K. α-Actinin structure and regulation. *Cell. Mol. Life Sci.* **65**, 2688–2701 (2008).
30. Hariadi, R. F., Cale, M. & Sivaramakrishnan, S. Myosin lever arm directs collective motion on cellular actin network. *Proc. Natl Acad. Sci. USA* **111**, 4091–4096 (2014).
31. Mattila, P. K. & Lappalainen, P. Filopodia: molecular architecture and cellular functions. *Nat. Rev. Mol. Cell Biol.* **9**, 446–454 (2008).
32. Rizvi, S. A. *et al.* Identification and characterization of a small molecule inhibitor of formin-mediated actin assembly. *Chem. Biol.* **16**, 1158–1168 (2009).
33. Nolen, B. J. *et al.* Characterization of two classes of small molecule inhibitors of Arp2/3 complex. *Nature* **460**, 1031–1034 (2009).
34. Suraneni, P. *et al.* The Arp2/3 complex is required for lamellipodia extension and directional fibroblast cell migration. *J. Cell Biol.* **197**, 239–251 (2012).
35. Wu, C. *et al.* Arp2/3 is critical for lamellipodia and response to extracellular matrix cues but is dispensable for chemotaxis. *Cell* **148**, 973–987 (2012).
36. Straight, A. F. *et al.* Dissecting temporal and spatial control of cytokinesis with a myosin II inhibitor. *Science* **299**, 1743–1747 (2003).
37. Uehata, M. *et al.* Calcium sensitization of smooth muscle mediated by a Rho-associated protein kinase in hypertension. *Nature* **389**, 990–994 (1997).
38. Hoffman, L. M. *et al.* Genetic ablation of zyxin causes Mena/VASP mislocalization, increased motility, and deficits in actin remodeling. *J. Cell Biol.* **172**, 771–782 (2006).
39. Djinovic-Carugo, K., Young, P., Gautel, M. & Saraste, M. Structure of the α-actinin rod: molecular basis for cross-linking of actin filaments. *Cell* **98**, 537–546 (1999).
40. Choi, C. K. *et al.* Actin and α-actinin orchestrate the assembly and maturation of nascent adhesions in a myosin II motor-independent manner. *Nat. Cell Biol.* **10**, 1039–1050 (2008).
41. Roca-Cusachs, P. *et al.* Integrin-dependent force transmission to the extracellular matrix by α-actinin triggers adhesion maturation. *Proc. Natl Acad. Sci. USA* **110**, E1361–E1370 (2013).
42. Low, S. H., Mukhina, S., Srinivas, V., Ng, C. Z. & Murata-Hori, M. Domain analysis of α-actinin reveals new aspects of its association with F-actin during cytokinesis. *Exp. Cell Res.* **316**, 1925–1934 (2010).

43. Kozlov, M. M. & Bershadsky, A. D. Processive capping by formin suggests a force-driven mechanism of actin polymerization. *J. Cell Biol.* **167,** 1011–1017 (2004).

44. Shemesh, T. & Kozlov, M. M. Actin polymerization upon processive capping by formin: a model for slowing and acceleration. *Biophys. J.* **92,** 1512–1521 (2007).

45. Cramer, L. P., Siebert, M. & Mitchison, T. J. Identification of novel graded polarity actin filament bundles in locomoting heart fibroblasts: implications for the generation of motile force. *J. Cell Biol.* **136,** 1287–1305 (1997).

46. Paul, A. S. & Pollard, T. D. Review of the mechanism of processive actin filament elongation by formins. *Cell Motil. Cytoskeleton* **66,** 606–617 (2009).

47. Breitsprecher, D. & Goode, B. L. Formins at a glance. *J. Cell Sci.* **126,** 1–7 (2013).

48. Xu, Y. *et al.* Crystal structures of a Formin Homology-2 domain reveal a tethered dimer architecture. *Cell* **116,** 711–723 (2004).

49. Shemesh, T., Otomo, T., Rosen, M. K., Bershadsky, A. D. & Kozlov, M. M. A novel mechanism of actin filament processive capping by formin: solution of the rotation paradox. *J. Cell Biol.* **170,** 889–893 (2005).

50. Mizuno, H. *et al.* Rotational movement of the formin mDia1 along the double helical strand of an actin filament. *Science* **331,** 80–83 (2011).

51. Courtemanche, N., Lee, J. Y., Pollard, T. D. & Greene, E. C. Tension modulates actin filament polymerization mediated by formin and profilin. *Proc. Natl Acad. Sci. USA* **110,** 9752–9757 (2013).

52. Jegou, A., Carlier, M. F. & Romet-Lemonne, G. Formin mDia1 senses and generates mechanical forces on actin filaments. *Nat. Commun.* **4,** 1883 (2013).

53. Soranno, T. & Bell, E. Cytostructural dynamics of spreading and translocating cells. *J. Cell Biol.* **95,** 127–136 (1982).

54. Speder, P., Adam, G. & Noselli, S. Type ID unconventional myosin controls left–right asymmetry in *Drosophila*. *Nature* **440,** 803–807 (2006).

55. Hozumi, S. *et al.* An unconventional myosin in *Drosophila* reverses the default handedness in visceral organs. *Nature* **440,** 798–802 (2006).

56. Speder, P. & Noselli, S. Left–right asymmetry: class I myosins show the direction. *Curr. Opin. Cell Biol.* **19,** 82–87 (2007).

57. Naganathan, S. R., Furthauer, S., Nishikawa, M., Julicher, F. & Grill, S. W. Active torque generation by the actomyosin cell cortex drives left–right symmetry breaking. *eLife* **3,** e04165 (2014).

58. Fürthauer, S., Strempel, M., Grill, S. W. & Jülicher, F. Active chiral processes in thin films. *Phys. Rev. Lett.* **110,** 048103 (2013).

METHODS

Cell culture and transfection. Human foreskin fibroblasts (HFFs) from the American Type Culture Collection (catalogue no. SCRC-1041) were cultured in Dulbecco's modified Eagle's medium high glucose supplemented with 10% fetal bovine serum (FBS), 1 mM sodium pyruvate and antibiotics (penicillin and streptomycin) at 5% CO_2 at 37 °C. Cells were transfected with DNA plasmids using electroporation (Neon transfection system, Life Technologies) following the manufacturer's instructions. The electroporation condition consists of two pulses of 1,150 V for 30 ms. Expression vectors encoding the following fluorescent fusion proteins were used: LifeAct–GFP (gift from R. Wedlich-Soldner, Max Planck Institute of Biochemistry, Martinsried, Germany), tdTomato–F-tractin (gift from M. J. Schell, Uniformed Services University, Bethesda, Maryland), GFP–actin (CLONTECH Laboratories), mCherry–paxillin (gift from S. Hanks, Vanderbilt University, Nashville, Tennessee), RFP–zyxin and GFP–tubulin (gift from I. Kaverina, Vanderbilt University Medical Center, Nashville, Tennessee), GFP–VASP (gift from B. M. Jockush, Technische Universität Braunschweig, Braunschweig, Germany), GFP–α-actinin-1 (gift from C. Otey, University of North Carolina, Chapel Hill, North Carolina), GFP–ABDdel-α-actinin-1 and SR12–GFP (gift from P. Roca-Cusachs, University of Barcelona, Barcelona, Spain). All cell culture and transfection reagents were obtained from Invitrogen. All chemicals and reagents were obtained from Sigma, unless otherwise stated.

Transfection of siRNA and immunoblotting. Cells were seeded into a 35 mm dish on day 0 and transfected with 20 μM of α-actinin-1 siRNA (Dharmacon, ON-TARGETplus SMARTpool siRNA, catalogue no. L-011195-00-0005) using Lipofectamine RNAiMAX (Invitrogen) on day 1 and day 2. Control cells were transfected with scrambled control siRNA (Dharmacon, ON-TARGETplus Non-targeting pool siRNA, catalogue no. D-001810-10). Transfection of plasmid by means of electroporation was performed on day 3 and cells were imaged on day 4. Transfected cells were lysed in RIPA buffer on day 4 and proteins extracted were separated by 4–20% SDS–polyacrylamide gel (Thermo Fisher Scientific) and transferred to PVDF membranes (Bio-Rad) at 100 V for 1 h and blocked for 1 h with 5% non-fat milk (Bio-Rad) before incubation at 4 °C overnight with appropriate primary antibodies: anti-α-actinin-1 (Abcam, catalogue no. ab81265, dilution 1:1,000, clone EP2528Y) and anti-α-actinin-4 (Enzo Life Sciences, catalogue no. ALX-210-356, dilution 1:2,500). Anti-α-tubulin (Sigma, catalogue no. T6199, dilution 1:5,000, clone DM1A) was used as an internal control. The primary antibody binding was processed for ECL detection (Bio-Rad) with appropriate HRP-conjugated secondary antibodies (Santa Cruz Biotechnology, catalogue no. sc-2004/5, dilution 1:10,000).

Micro-contact printing. Micro-contact printing was performed as previously described with some modifications[59]. The photoresist master mould for the stamp was produced using an ultraviolet lithography technique by illuminating a negative photoresist (SU8 3010, Microchem) through a chrome sodalime photomask on which circular micropatterns of 1,800 μm² were written by a laser writer system. The area of the circular island was chosen to guarantee that cells would spread over the entire island by the time observations were started (∼20 min after re-plating), but would not undergo elongation and shape changes. The obtained photoresist master mould was then exposed to trichloro(1H,1H,2H,2H-perfluorooctyl)silane in vapour-phase to prevent polydimethylsiloxane (PDMS) adhesion. PDMS (Sylgard 184 kit, Dow Corning) was finally cast on the photoresist mould using a 10:1 ratio (w/w) of elastomer to crosslinker and cured for 2 h at 80 °C. The crosslinked PDMS layer was peeled off and stamps were cut out manually. The PDMS stamp was activated in the plasma chamber (CUTE, Femto Science) for 4 min under a weak flow of air and inked for 5 min with a 100 μg ml⁻¹ fibronectin solution (Calbiochem, Merck Millipore) containing 1% of Cy5-conjugated fibronectin. After aspiration of the fibronectin solution, the stamp was dried under filtered airflow and stamped onto the plastic bottom of 35-mm ibidi's hydrophobic uncoated μ-dishes (ibidi GmbH). The stamp was pressed slightly with tweezers for several seconds and remained in contact with the dish for an additional 5 min. After the removal of the stamp, the printed dish bottom was washed once with 1× PBS and passivated with 0.2% Pluronic acid–H_2O for 10 min. The passivated dishes were washed twice with 1× PBS before cell seeding.

Drug treatment. For drug inhibition studies, cells were pre-treated with 1 μM nocodazole, 10 μM SMIFH2 (ChemBridge Corporation) or 100 μM CK666 respectively in DMEM containing serum for 3 h at 5% CO_2 at 37 °C before trypsinization. For myosin-II-driven contractility inhibition studies, 30 μM Rho-kinase inhibitor Y-27632 or 50 μM blebbistatin was added for 10 min to suspended cells before cell seeding. All inhibitors remained in the medium during the entire period of observation, except in drug washout experiments.

Immunofluorescence antibody staining. Cells were fixed and simultaneously permeabilized at 37 °C in a mixture of 3% paraformaldehyde–PBS, 0.25% Triton-X-100 and 0.2% glutaraldehyde for 15 min, and then washed twice with 1× PBS for 10 min each time. Before staining, treatment with 1 mg ml⁻¹ sodium borohydride in cytoskeleton buffer (10 mM MES, 150 mM NaCl, 5 mM EGTA, 5 mM $MgCl_2$, 5 mM glucose, pH 6.1) for 15 min on ice was performed. Fixed cells were blocked with 1% bovine serum albumin (BSA)-PBS for 1 h at room temperature before incubation with appropriate primary antibodies: anti-paxillin (Sigma, catalogue no. P1093, dilution 1:200, clone PXC-10); anti-vinculin (Sigma, catalogue no. V9131, dilution 1:200, clone hVIN-1); anti-myosin IIA (Covance, catalogue no. PRB-440P, dilution 1:500); anti-α-actinin-1&4 (Sigma, catalogue no. A5044, dilution 1:200, clone BM-75.2) or anti-α-actinin-1 (US Biological, catalogue no. A0761-02F, dilution 1:200) at room temperature for 1 h. Cells were then incubated for 1 h at room temperate with appropriate AlexaFluor-conjugated secondary antibodies (Molecular Probes, dilution 1:400). Actin staining was performed using phalloidin (Molecular Probes).

Live cell imaging and confocal microscopy. Cells were trypsinized 24 h after transfection and seeded at a density of 5×10^4 cells ml⁻¹ onto printed dishes. Unattached cells were removed with a 1× PBS wash 10–20 min after cell seeding before proceeding to imaging. Cells were imaged in Leibovitz's L-15 containing 10% FBS at 5% CO_2 at 37 °C. Time-lapse images at 2–5 min intervals and Z-stack images of step-size 0.35 μm (total height, 10–15 μm) were acquired with a spinning-disc confocal microscope (PerkinElmer Ultraview VoX) attached to an Olympus IX81 inverted microscope, equipped with a ×10 oil immersion objective (1.40 NA, UPlanSApo), an EMCCD camera (C9100-13, Hamamatsu Photonics) for image acquisition, and Volocity software (PerkinElmer) to control the set-up. Fixed samples were also imaged with a Nikon A1R system attached to a Nikon Ti-E inverted microscope with a ×100 oil immersion objective (1.40 NA, CFI Plan-ApochromatVC), and an Andor Neo sCMOS camera (Andor Technology) with Nikon NIS-Elements AR software to control the set-up or a Zeiss LSM710 system attached to a Zeiss Observer Z1 inverted microscope with a ×100 oil immersion objective (1.46 NA, Plan-Apochromat) with Zen software to control the set-up.

Correlative light and electron microscopy. HFF cells were grown on carbon-coated Formvar 100 mesh finder grids (EMS). Micro-contact printing onto the carbon-coated Formvar was carried out as above, with the following modification to accommodate the TEM substrate here. After the removal of the PDMS stamp, the printed carbon-coated Formvar was washed once with 1× PBS and passivated with 0.2 mg ml⁻¹ polyethylene glycol (PEG)–poly-L-lysine for 2 h at room temperature. Epifluorescence images of fixed cells were acquired on an inverted light microscope (Eclipse TE 2000-U, Nikon) equipped with a manual controlled shutter, filter wheels, and a 14-bit cooled CCD camera (Orca II) controlled by MetaMorph software (Universal Imaging) by a Plan Fluor ELWD ×40/0.60 Ph2 or Plan Fluor ×10/0.30 Ph1 objective lens (Nikon). Viewing a large number of cells on a single grid, by using the grid finders, allows for localization of the exact individual cell in both light and electron microscope imaging. Cells were chemically fixed in cytoskeleton buffer containing 4% PFA, washed, and stained with aqueous 2% OsO_4 and 2% uranyl acetate. Dehydration in increasing concentrations of reagent-grade ethanol (15%, 20%, 50%, 70%, 95%, and 100%; 3 min per change) was followed by drying from liquid CO_2 by the critical-point method according to refs 60,61. Images were obtained under low-dose conditions with a TecnaiG2 F20 microscope (FEI Company) equipped with FEG at 200 keV. Kodak SO-163 plates were developed for 13 min by using D19 developer (Eastman Kodak).

Electron tomography, image analysis and modelling. Tomographic tilt series (approximately −70 to +70°, every 2°) were acquired on a Tecnai G2 F20 (FEI Company) equipped with an energy filter (zero-loss, Gatan) using a 2020 advanced tomography holder (Fischione Instruments). The data were collected using SerialEM (ref. 62). Three-dimensional reconstructions were generated using alignment and back-projection algorithms implemented in the IMOD package[63]. Modelling was done in Blender (www.blender.org).

Cytoskeleton probing with myosin-V- and myosin-VI-coated nanoparticles. Myosin V and VI were prepared as previously described[64,65]. DNA origami was prepared as previously described[66]. All myosin proteins were expressed with carboxy-terminal fusions of alkyl-guanine-transferase (AGT; SNAP tag). SNAP tags were linked to benzyl-guanine-labelled oligonucleotides (standard New England Biolabs protocol) with complementary sequences to sites of attachment designed on the DNA origami. Purified DNA origami were mixed with an excess of oligo-labelled myosin and incubated for 20 min at 37 °C. DNA origami conjugated with either myosin V or VI proteins were separated from unconjugated myosin by affinity purification. Each DNA origami was conjugated with 6 myosin V or 6 myosin VI. Myosin-V- and myosin-VI-coated nanoparticles were immediately used in motility assays. HFFs were permeabilized as previously described[67] with some modifications. Cells were washed gently with 85% PBS before treatment with extraction buffer

(50 mM imidazole, pH 6.8, 50 mM KCl, 0.5 mM MgCl$_2$, 0.1 mM EDTA and 1 mM EGTA) containing 1% Triton-X-100, 4% PEG (relative molecular mass 35,000) and 250 nM AlexaFluor-488–phalloidin (Invitrogen) for 4 min at room temperature. Extracted cells were then washed once with extraction buffer containing 250 nM unlabelled phalloidin and three times with 1× PBS containing 250 nM unlabelled phalloidin. This was followed by fixation in 2% formaldehyde (Tousimis) for 9 min at room temperature and three washes with 1× PBS containing 250 nM unlabelled phalloidin. Fixed extracted cells were stored in 1× PBS containing 1 mg ml^{-1} BSA and 250 nM AlexaFluor-488–phalloidin at 4 °C before use in motility assay. AlexaFluor-488–phalloidin stabilized HFF actin networks were incubated with myosin-V- or -VI-coated nanoparticles under standard motility buffer (20 mM imidazole pH 7.4, 25 mM KCl, 0.5 mM EGTA, 1 mM dithiothreitol, 1 mg ml^{-1} BSA, 2 mM ATP, 9.0 µM calmodulin, 1 mM phosphocreatine, 0.1 mg ml^{-1} creatine-phospho-kinase, 25 µg ml^{-1} glucose-oxidase, 45 µg ml^{-1} catalase and 1% glucose). Movements of myosin-V- or -VI-coated nanoparticles on HFF actin networks were acquired at 2 Hz for 2–10 min per field of view. Images were acquired on a Nikon Ti-E inverted microscope, equipped with a ×100 oil immersion objective (1.40 NA, Plan- Apochromat), a ×1.5 magnifier, a mercury arc lamp and an EMCCD camera (Evolve, Photometrics), controlled by Nikon NIS-Elements software.

Cell permeabilization and cytoskeleton contractility assay. HFFs were permeabilized as previously described[68]. Briefly, cells were permeabilized with buffer M (50 mM imidazole, pH 6.8, 50 mM KCl, 0.5 mM MgCl$_2$, 0.1 mM EDTA, l mM EGTA and l mM 2-mercaptoethanol) supplemented with 0.1% Triton-X-100, 4% PEG (relative molecular mass 35,000), 250 nM AlexaFluor-488–phalloidin and 2 µl ml^{-1} protease inhibitors cocktail (Sigma, catalogue no. P8340) for 10 min at room temperature. After permeabilization, cells were washed three times with buffer M supplemented with protease inhibitors. The cytoskeleton contractility assay of the AlexaFluor-488–phalloidin stabilized HFF actin networks was carried out at 37 °C in buffer M supplemented with 250 nM unlabelled phalloidin, 13.2 nM AlexaFluor-488–phalloidin and protease inhibitors containing 2 mM ATP alone or together with the appropriate drug. Experiments were also performed in the absence of ATP or in the presence of 2 mM AMPPNP in place of ATP. For drug treatment, cells were incubated in either 100 µM blebbistatin, 1 µM jasplakinolide or 1 µM latrunculin A in buffer M supplemented with protease inhibitors for 10 min before conducting the cytoskeleton contractility assay. All inhibitors remained in the medium during the entire period of observation.

Photobleaching and measurement of the translocation rate of the bleach zone and the TF. The photobleaching experiment was performed on the Nikon A1R system mentioned above. The ring-shape bleaching pattern was drawn using the Nikon NIS-Elements AR software. The 488 nm laser line was used for GFP visualization as well as for photobleaching. Five consecutive images of the cell were captured before bleaching. Bleaching was performed using 100% laser power for 32 s. Images of the cell were collected every 10 s for 3 min following photobleaching. A region of interest containing a photobleached RF, together with an interacting TF, was used for generation of a kymograph (see Fig. 4b). The TF was visualized as a bright band in the kymograph; the bleached zone was visualized as a dark band. Automated tracking of the bleached zone and the TF was performed using Igor Pro 6 (WaveMetrics) with a custom script (available online at http://www.igorexchange.com/project/ActinFiberShiftAnalysis). To detect TF movement, the algorithm applied a Gaussian fit to each column on the kymograph, getting an array of central positions of peaks. A second algorithm used a step-hunting method to detect bleach zone movement. By performing least χ-square two- or three-step fitting[69] to signals along each column, the edge position of the dark band could be identified. Cross-correlation of each sub-region to its first frame revealed the change of the fibres' position in sub-pixel resolution[70]. Consequently, we had a plot of the distance moved over time of both the bleached zone and TF, from which the velocities of centripetal movement of TR and RF growth were calculated.

Image processing and data analysis. Maximum projection of the time-series Z-stack images was performed with Volocity software or with ImageJ (National Institutes of Health, NIH) and exported as TIFF files. All subsequent image processing and analysis were performed with ImageJ or Imaris (Bitplane Scientific Software). Image analysis of moving myosin-coated nanoparticles was performed using Custom MATLAB Particle Tracking software as previously described[67]. Trajectories of individual nanoparticles were analysed using Custom MATLAB Particle Tracking software. A two-dimensional Gaussian fit was used to estimate nanoparticle position with sub-pixel resolution. The image of the overall trajectory tracks found within the cell was prepared using Imaris. Maximum-projection images of GFP–α-actinin-1, GFP–ABDdel-α-actinin-1, GFP–VASP or RFP–zyxin were used for intensity measurement using the measure function in ImageJ. Level of fusion protein expression was estimated by measuring the intensity of either GFP or RFP fluorescence (arbitrary unit, a.u.) per square micrometre of cell area and subtracting the background level. Background level was estimated by measuring the intensity of the fluorescence per square micrometre outside the cell area. Angle (°) of actin fibre tilt was measured as depicted in Fig. 6c using the 'angle tool' in ImageJ.

Repeatability of experiments. The numbers of independent experiments performed for all of the quantitative data are specified in the figure legends. Images in Figs 1a,b, 2a,b and 6a and Supplementary Fig. 7 are representative of more than three independent experiments. Images in Figs 4a–c, 5 and 7d,f, and Supplementary Figs 1a,c, 4 and 5b are representative of three independent experiments. Images in Figs 3a–f and 7a, and Supplementary Figs 3a–e and 6a,b are representative of two independent experiments. Images in Fig. 2c–g and Supplementary Fig. 2a–f are obtained in a single experiment. The immunoblot in Fig. 7c is representative of three independent experiments. Computer simulation in Fig. 8b is representative of more than 50 simulation runs. All supplementary videos show representative data from at least three independent experiments, except for Supplementary Videos 5, 6 and 12, which were from two independent experiments and Supplementary Video 4 was from a single experiment. Supplementary Videos 15–18 are simulation videos.

Statistical analyses. Prism (GraphPad Software) was used for analysis. Analyses of significant differences were carried out using two-tailed unpaired Student's t-test or, when more than two groups were assessed, by one-way ANOVA with Bonferroni *post hoc* correction. We used the D'Agostino–Pearson test to assess normality. As recommended by the software, a Mann–Whitney test was used when normality was not achieved. An F-test was used to compare variance. If variance is significantly different, an unpaired t-test with Welch's correction was performed as recommended by the software. The methods for statistical analysis and numbers of samples (n) measured are specified in the figure legends for all of the quantitative data. Differences were accepted as significant for $P < 0.05$. No statistical method was used to predetermine sample size.

59. Thery, M., Pepin, A., Dressaire, E., Chen, Y. & Bornens, M. Cell distribution of stress fibres in response to the geometry of the adhesive environment. *Cell Motil. Cytoskeleton* **63,** 341–355 (2006).
60. Anderson, T. F. Techniques for the preservation of 3-dimensional structure in preparing specimens for the electron microscope. *Trans. N. Y. Acad. Sci.* **13,** 130–134 (1951).
61. Buckley, I. K. & Porter, K. R. Electron-microscopy of critical-point dried whole cultured-cells. *J. Microsc.* **104,** 107–120 (1975).
62. Mastronarde, D. N. Automated electron microscope tomography using robust prediction of specimen movements. *J. Struct. Biol.* **152,** 36–51 (2005).
63. Kremer, J. R., Mastronarde, D. N. & McIntosh, J. R. Computer visualization of three-dimensional image data using IMOD. *J. Struct. Biol.* **116,** 71–76 (1996).
64. Bryant, Z., Altman, D. & Spudich, J. A. The power stroke of myosin VI and the basis of reverse directionality. *Proc. Natl Acad. Sci. USA* **104,** 772–777 (2007).
65. Rock, R. S., Rief, M., Mehta, A. D. & Spudich, J. A. *In vitro* assays of processive myosin motors. *Methods* **22,** 373–381 (2000).
66. Rothemund, P. W. K. Folding DNA to create nanoscale shapes and patterns. *Nature* **440,** 297–302 (2006).
67. Sivaramakrishnan, S. & Spudich, J. A. Coupled myosin VI motors facilitate unidirectional movement on an F-actin network. *J. Cell Biol.* **187,** 53–60 (2009).
68. Tint, I. S., Hollenbeck, P. J., Verkhovsky, A. B., Surgucheva, I. G. & Bershadsky, A. D. Evidence that intermediate filament reorganization is induced by Atp-dependent contraction of the actomyosin cortex in permeabilized fibroblasts. *J. Cell Sci.* **98,** 375–384 (1991).
69. Kerssemakers, J. W. *et al.* Assembly dynamics of microtubules at molecular resolution. *Nature* **442,** 709–712 (2006).
70. Gelles, J., Schnapp, B. J. & Sheetz, M. P. Tracking kinesin-driven movements with nanometre-scale precision. *Nature* **331,** 450–453 (1988).
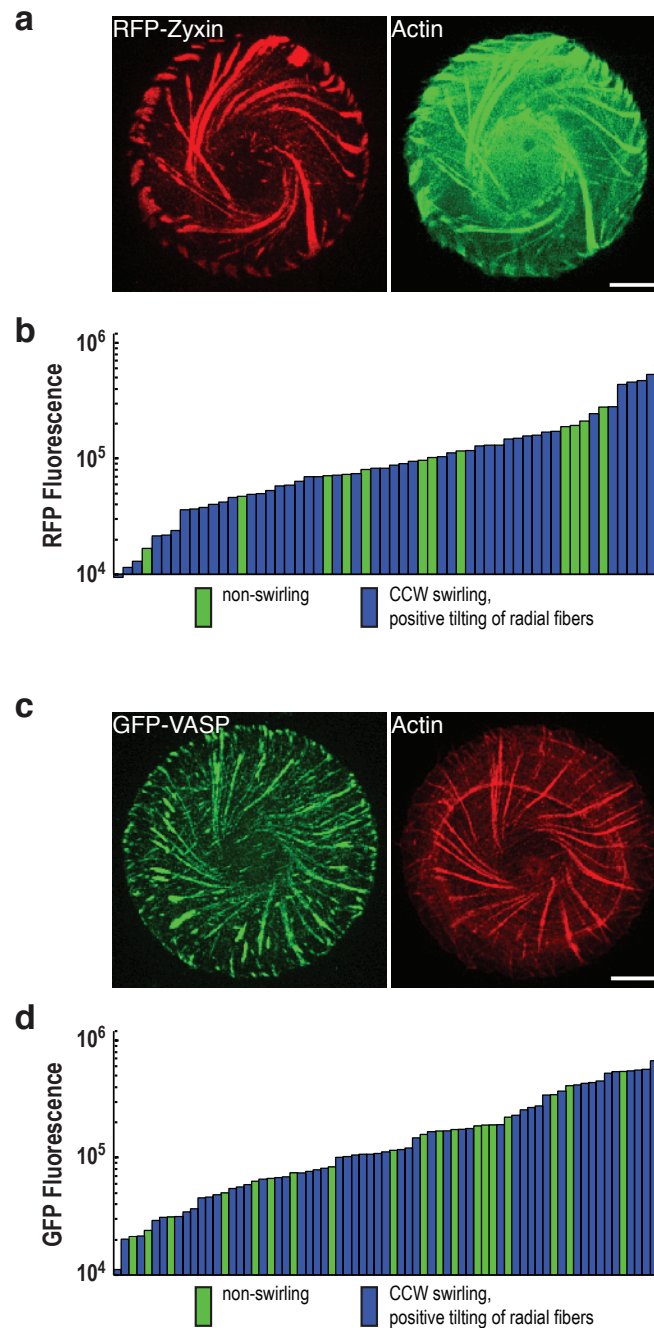
Supplementary Figure 1 Overexpression of radial fiber components, Zyxin or VASP, is not sufficient to reverse chirality. RFP-Zyxin **(a)** and GFP-VASP **(c)** localized to radial fibers and focal adhesions. Actin was visualized either by co-transfection with LifeAct-GFP (green in **a**) or phalloidin staining (red in **c**). Scale bars, 10 μm. RFP-Zyxin **(b)** or GFP-VASP **(d)** expressing cells were filmed to follow their actin dynamics. The expression level in an individual cell was assessed by measuring either total RFP or total GFP fluorescence intensity respectively. The y-axis represents fluorescence intensity in a log scale; the cells were sorted in ascending order of their respective protein expression level along the x-axis. Each bar on the histogram represents an individual cell. Color-coding indicates the type of actin cytoskeleton dynamics for each cell. Green – cells that do not demonstrate swirling during the entire period of observation (~10 hours). Blue – cells demonstrating positive tilt of radial fibers and counter-clockwise swirling similar to control cells. No clockwise swirling events were observed in these experiments. 58 cells assessed for RFP-Zyxin, and 72 cells assessed for GFP-VASP.
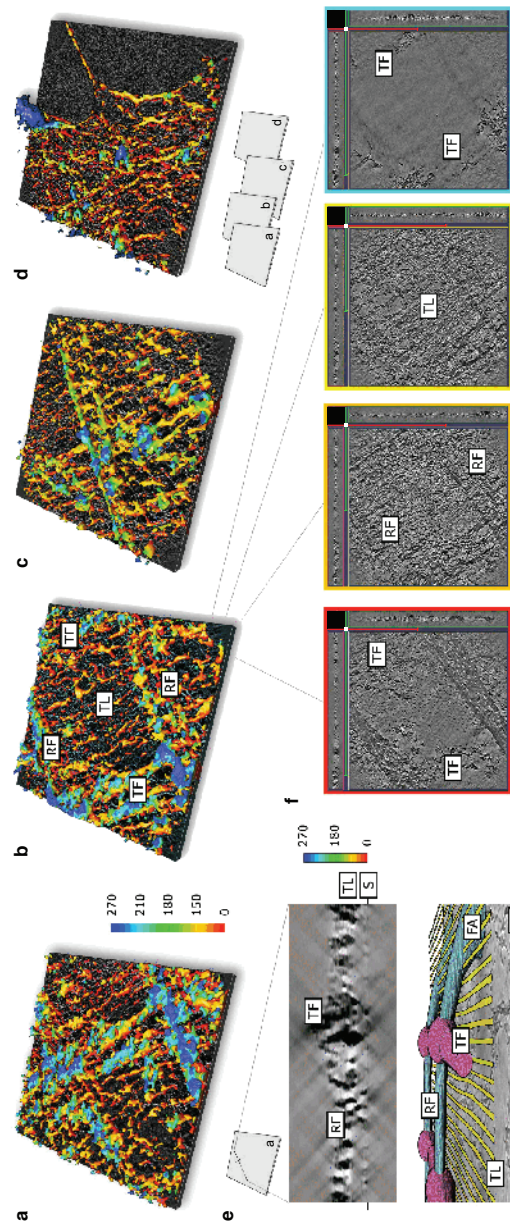
Supplementary Figure 2 Electron tomography showing 3D morphology and organization of transverse and radial fibers. **(a-d)** Surface representations of overlapping 3D electron tomographic reconstructions running along radial fibers. The relative spatial arrangement of the four reconstructions is shown below **d**. The center of the cell is towards the left of **a**, while the cell edge is shown in **d**. The height (in nm) of the features are mapped according to the color key on the right of **a**. The area of a reconstructed image is 2.8 μm². Radial (RF) and transverse (TF) fibers as well as the transversal layer (TL) are indicated in **b**. Nearer to the cell center (**a,b**), the transverse and radial fibers (blue and cyan) are above the transversal layer (orange). Towards the cell edge (**c,d**), the two fiber systems move closer to the substrate (color shift from blue/cyan to cyan/green and green/orange) and finally appear below the orange transversal layer plane (in **d**) when the focal adhesions contact the substrate. **(e)** Cross-section of the reconstruction shown in **a**. The upper panel shows a 10 nm thick cross-section along the long axis of the radial fibers to the top of **a**, perpendicular to the transverse fibers, as indicated in the scheme at the upper left corner of **e**. The transverse layer (TL) and the substrate (S) locations are marked at the sides of the figure. The location

of the radial fiber (RF) and the location where the transverse fiber (TF) runs perpendicular to the image plane are also marked. Transverse fibers appear to interact with radial fibers. The height (in nm) is shown in the bar on the right. The bar is color-coded for comparison with **a-d**. The width of the cross-section is 1.9 μm. The components of the radial fibers go in and out of the cross-section, generating an alternating pattern of black and white regions. The lower panel shows the model derived from the tomographic reconstructions in a view similar to that in the upper panel for comparison. **(f)** XY slices through the tomographic reconstruction (each 2 nm thick) shown in **b** (see also Supplementary Video 4). The heights of the sections are indicated by the color of the rim, which correspond to the color-coding in **a** and **e**. Orthogonal side views are also shown for each slice on the top and to the right. The location of the XZ slices (top) within the XY view are indicated by the end of the red lines at the right of the XY view; the location of the YZ slices (right) are indicated by the end of the green lines at the top of the XY view. Radial fibers (RF), transversal layer (TL), as well as the top and bottom occurrences of the transverse fibers (TF) are marked on the slices. See also Supplementary Video 3 for comparison with fluorescence microscopy.
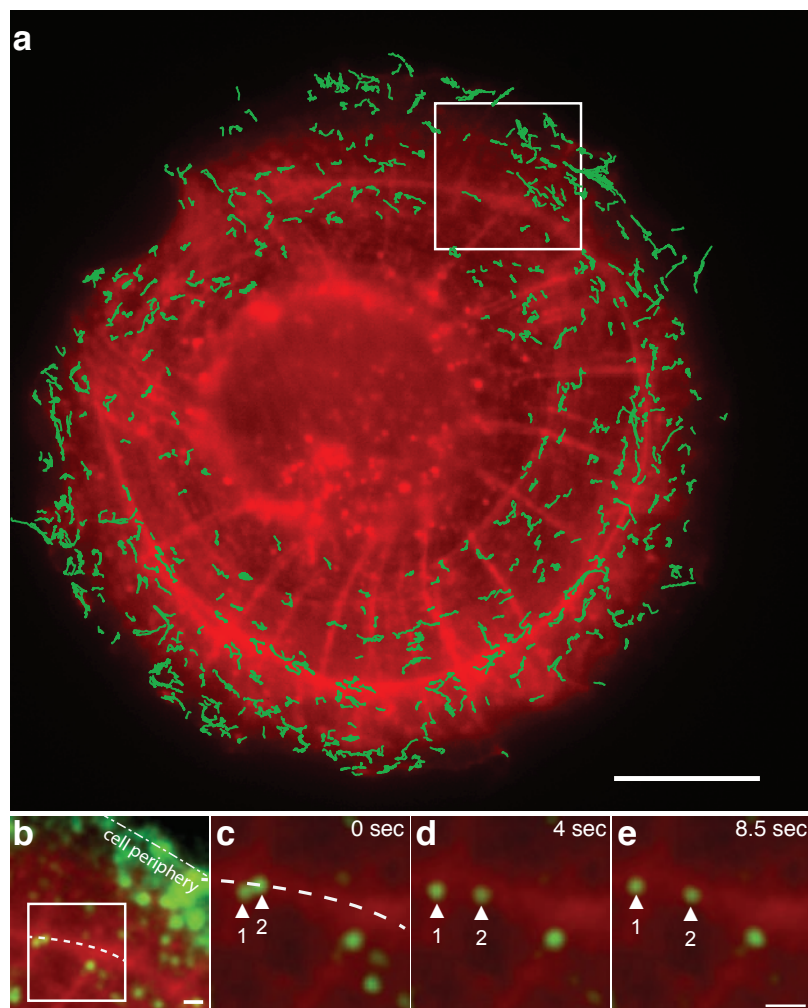
Supplementary Figure 3 Probing actin fibers in permeabilized cells with myosin VI-coated nanoparticles. **(a)** Movement trajectories (green) of fluorescent nanoparticles coated with myosin VI along the actin cytoskeleton (red) of a fixed extracted cell. The white box marks the view shown in **b**. Scale bar, 10 μm. **(b-e)** High magnification view of myosin VI nanoparticle movement along the single transverse fiber. **(b)** A view of actin cytoskeleton (red) after extraction. White-boxed region: The transverse fiber decorated with myosin VI nanoparticles (green) is marked by the dotted line. **(c-e)** Sequential images from the live imaging of myosin VI nanoparticles moving along the transverse fiber. Nanoparticles #1 and #2 (white arrowheads) are moving away from each other. Scale bars, 1 μm. The full-length sequence is shown in Supplementary Video 6.

Untreated control		Nocodazole-treated	
Actin	Microtubule	Actin	Microtubule
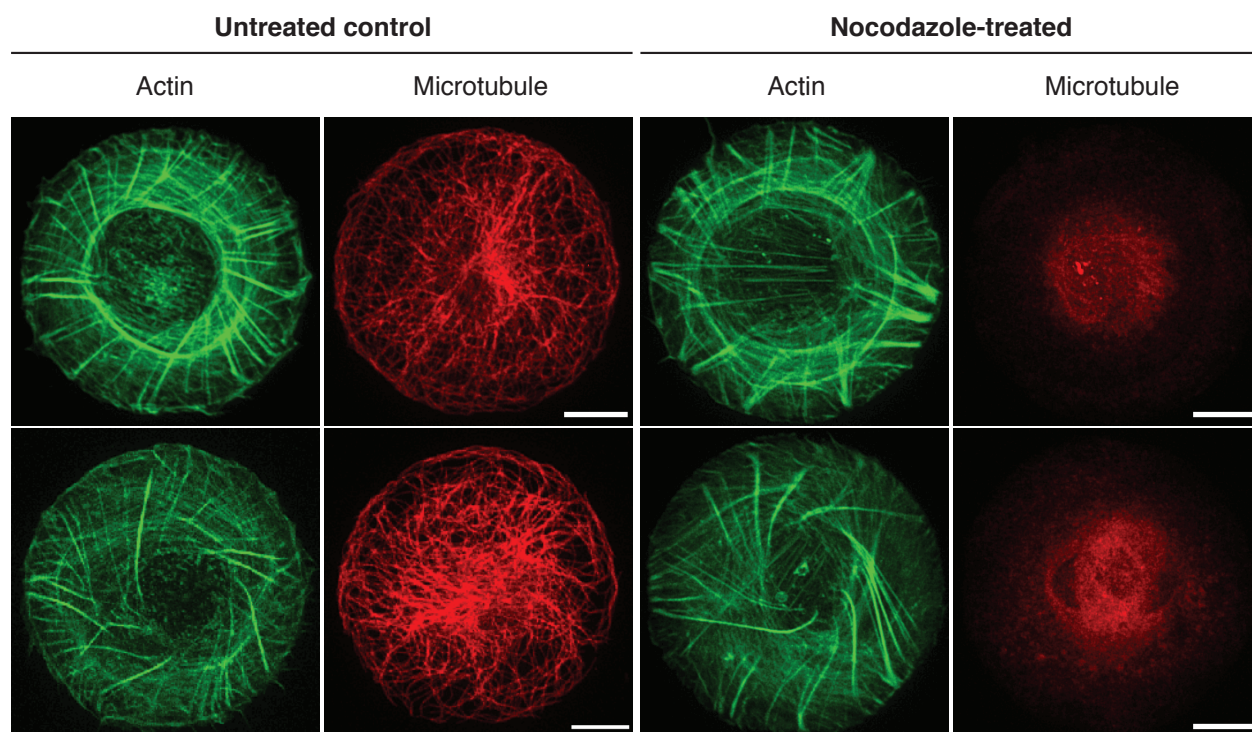
Supplementary Figure 4 Self-organization of the actin cytoskeleton in cells with depolymerized microtubules. Disruption of microtubules by nocodazole was confirmed by anti-α-tubulin immunofluorescence staining. Actin was visualized with phalloidin staining. The radial and chiral patterns of the actin cytoskeleton organization in cells with an intact microtubule system and in cells lacking microtubules are shown. Scale bars, 10 μm. See also Supplementary Video 10.

a

Actin binding Integrin
(ABD)   binding

α-Actinin-1: [CH][CH] [R1][R2][R3][R4][CaM]

Anti-parallel dimer of α-actinin-1

ABDdel-α-actinin-1: [R1][R2][R3][R4][CaM]

SR12: [R1][R2]

b

GFP-ABDdel-α-actinin-1   Vinculin

Myo-IIA   Actin

c

■ GFP-ABDdel-α-actinin-1 "single-ended" stress-fiber
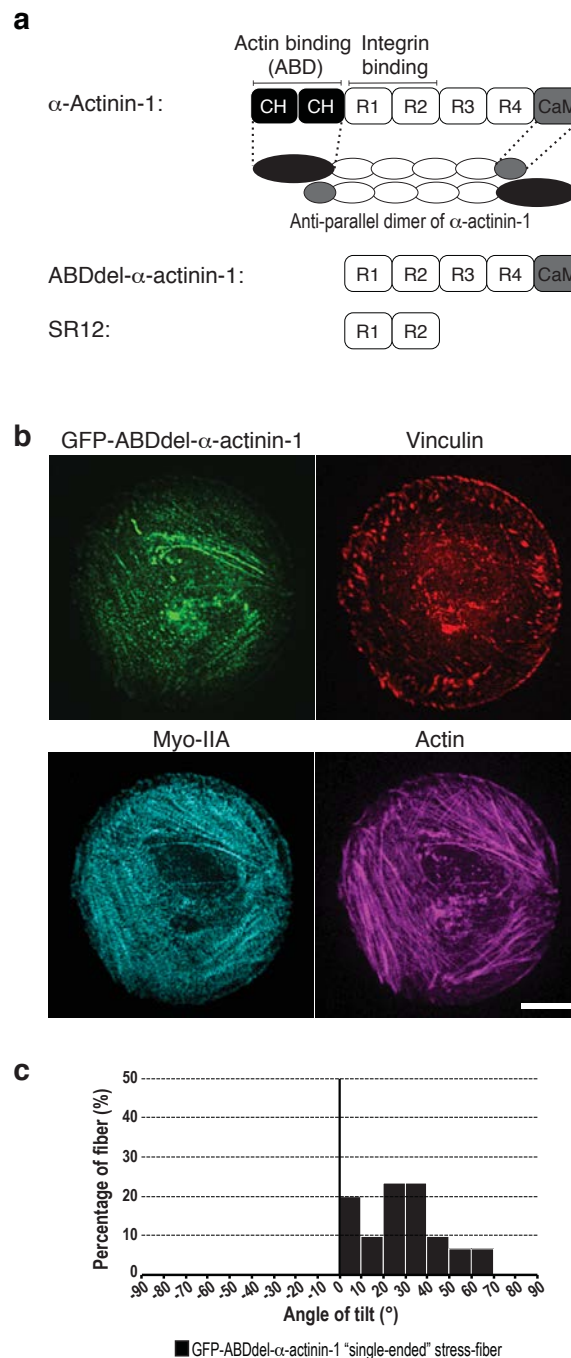
Supplementary Figure 5 Long "single-ended" stress-fibers replace radial fibers in GFP-ABDdel-α-actinin-1 expressing cells. **(a)** Schematic diagram illustrating the molecular organization of α-actinin-1 and its mutants. The α-actinin-1 monomer has an N-terminal actin-binding domain (ABD) composed of two calponin-homology (CH) domains, a central rod consisting of four spectrin repeats (R1-R4), and a C-terminal calmodulin (CaM)-like domain. α-actinin-1 monomers form an anti-parallel dimer with the ABD domain present at both ends. The ABDdel-α-actinin-1 mutant lacks the ABD domain[41]. Spectrin repeats 1 and 2 are responsible for integrin binding. The SR12 mutant consists only of these spectrin repeats (R1 and R2)[41]. **(b)** Cells expressing GFP-ABDdel-α-actinin-1 were extracted prior to fixation to reduce background due to the presence of excess soluble GFP-ABDdel-α-actinin-1. Truncated GFP-ABDdel-α-actinin-1 mutant protein localized to long actin fibers (purple). Unlike radial fibers, these fibers also contained myosin-IIA (blue). However, unlike ventral stress-fibers, they were associated with only one focal adhesion (labeled by vinculin, red). Thus, we classified this type of actin fibers as "single-ended" stress-fibers. Scale bar, 10 μm. **(c)** Histogram showing the distribution of "single-ended" actin fiber tilt angle (°) in a cell expressing GFP-ABDdel-α-actinin-1. 30 actin fibers of a representative cell were analyzed. See also Supplementary Video 12. Note that unlike radial fibers in cells overexpressing the full-length α-actinin-1, the "single-ended" stress-fibers in cells expressing GFP-ABDdel-α-actinin-1 tilt in the same direction as radial fibers in control cells (see Fig. 6c).
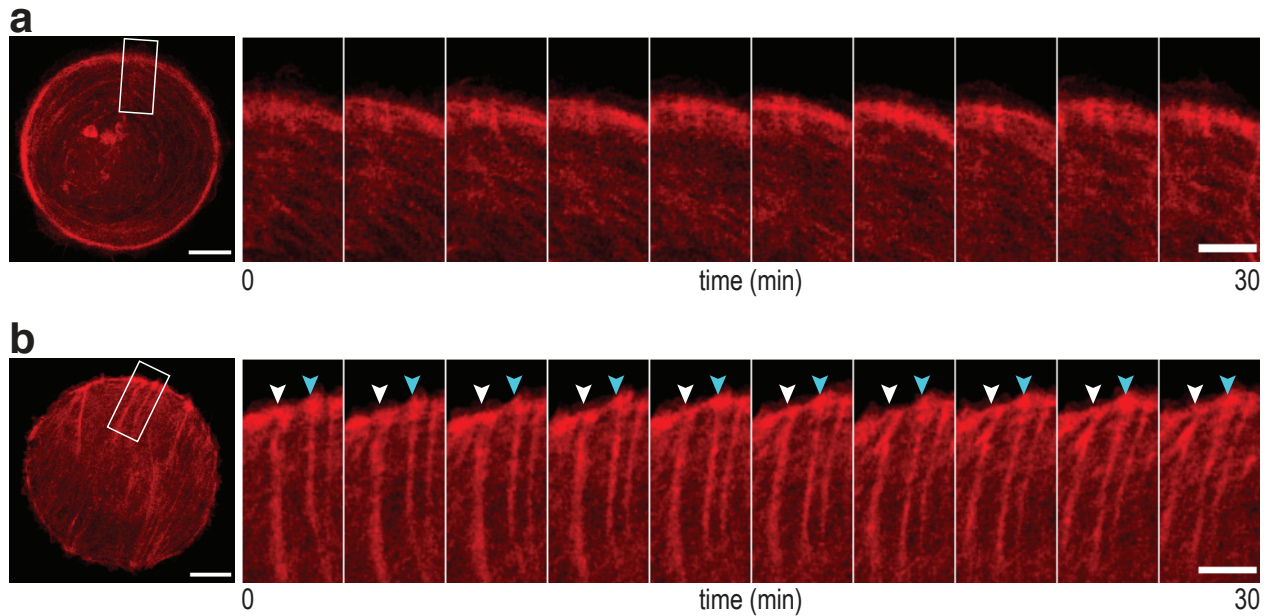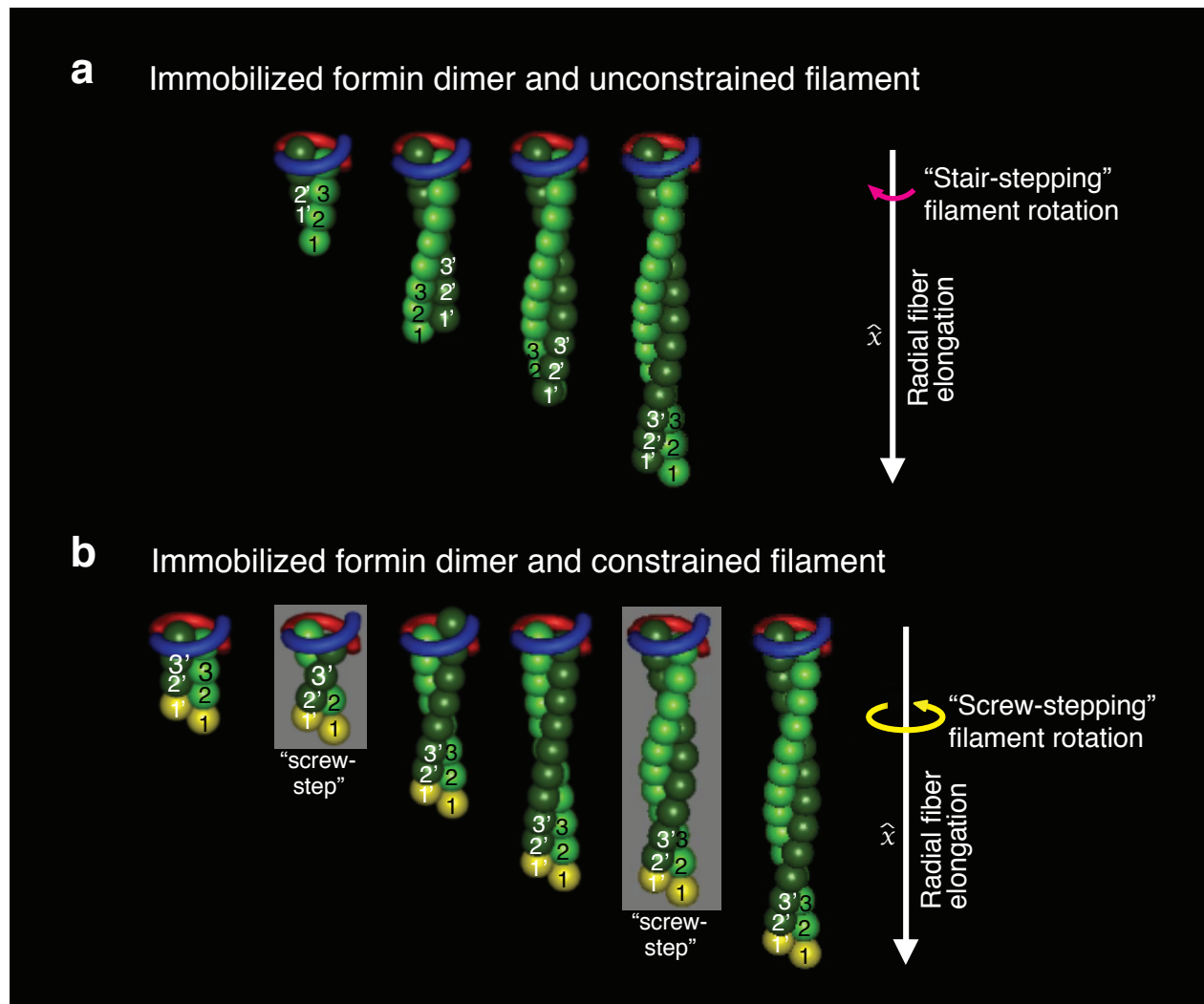
Supplementary Figure 6 The effect of SR12-GFP α-actinin-1 fragment on actin cytoskeleton self-organization. **(a,b)** Actin organization (visualized by tdTomato-F-Tractin) in SR12-GFP expressing cells and high magnification time-series images illustrating actin dynamics (white-boxed region). 60% of SR12-GFP transfected cells demonstrated phenotypes similar to control cells (30% counter-clockwise swirling and 30% non-swirling). The remaining 40% of the transfected cells were found to express a higher level (2-fold on average) of SR12-GFP. 60% of these higher SR12-GFP expressing cells failed to progress beyond the circular stage **(a)** while the remaining 40% exhibited similar behavior to GFP-ABDdel-α-actinin-1 mutant expressing cells, forming characteristic "single-ended" stress-fibers that tilt in a positive direction **(b)**. An example of two "single-ended" stress-fibers are shown here (white and cyan arrowheads). Scale bars, 10 μm; 5 μm (high-magnification). $n = 39$ transfected cells pooled from 2 independent experiments.
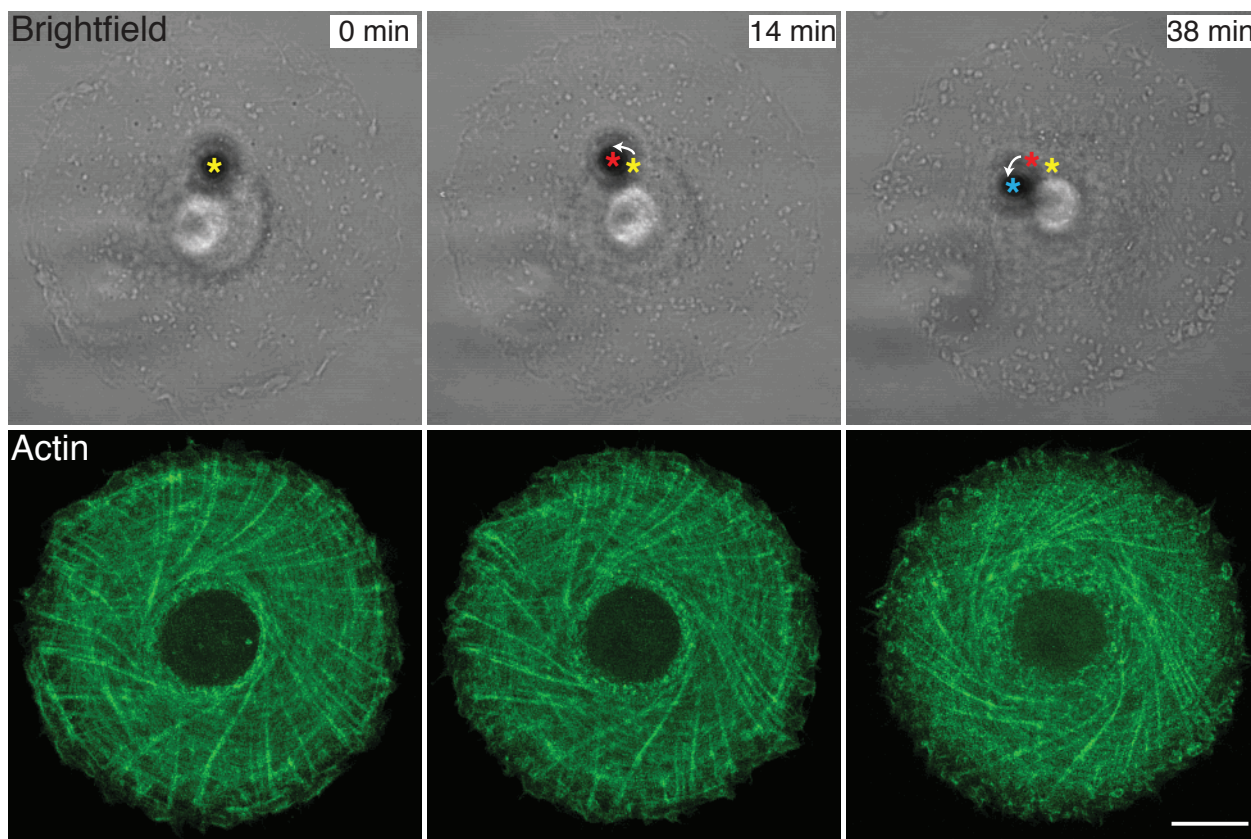
Supplementary Figure 7 Membrane-bound beads move in a chiral motion coupled to the swirling of the actin network. Fibronectin-coated beads (4.5 μm in diameter) moved in a counter-clockwise direction on the cell surface as the actin cytoskeleton swirled in the same direction. Yellow, red and cyan asterisks (*) marks the bead position at time points 0-, 14- and 38-minute respectively. The arrow indicates the direction of the bead movement. Scale bar, 10 μm.

a Immobilized formin dimer and unconstrained filament

"Stair-stepping" filament rotation

$\hat{x}$ Radial fiber elongation

b Immobilized formin dimer and constrained filament

"screw-step"

"screw-step"

"Screw-stepping" filament rotation

$\hat{x}$ Radial fiber elongation

Supplementary Figure 8 Schematic illustration depicting polymerization of individual actin filaments nucleated by formins. **(a)** Polarized actin filaments (green) capped by a formin dimer (blue-red). The first three actin subunits in the two actin helices are numbered 1-3 and 1'-3' respectively. The formin dimer is immobilized while the opposite end of the actin filament is not. Unconstrained actin filaments rotate in the positive angular direction about -axis (magenta arrow), as experimentally shown by Mizuno et al.[50] **(b)** Actin filaments are prevented from rotating via immobilization of barbed end by formin and trapping of opposite end by α-actinin cross-linking. Immobile actin subunits are labeled in yellow. Torsional elastic energy accumulated during polymerization is periodically released via high amplitude rotation ("screw-step" highlighted by gray background) in the negative direction (yellow arrow). See details in Shemesh et al.[49]. See also Supplementary Videos 17 and 18).
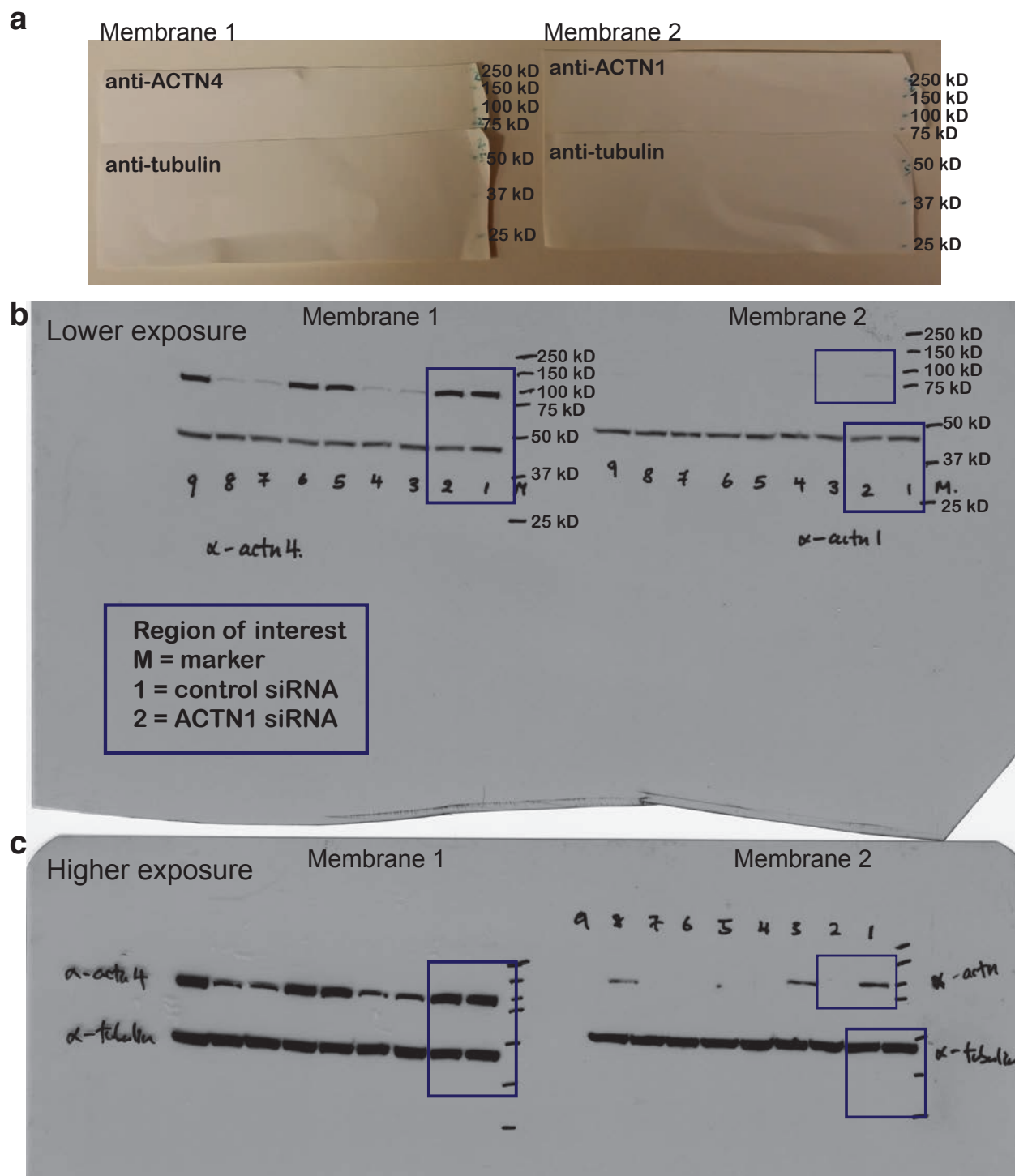
Supplementary Figure 9 Primary immunoblotting data **(a)** 10 μg samples of protein cell lysates from control siRNA- and ACTN1 siRNA-transfected cells were separated on SDS-PAGE gel and transferred to PVDF membranes. Positions of molecular weight markers are indicated to the right of each PVDF membrane. **(b)** Immunoblotting was performed with corresponding antibodies, anti-ACTN1, anti-ACTN4 and anti-α-tubulin, and developed using standard ECL procedure. Scans of uncropped immunoblot is shown here. Data from this immunoblot was used in Fig. 7c.

Supplementary Video Legends

Supplementary Video 1 A typical example of the self-organization of the actin cytoskeleton in cell on a circular adhesive island. Images were recorded at 2 minute intervals over a period of ~ 11 hours. Display rate is 30 frames/sec and corresponds to the time-lapse series in Fig. 1b.

Supplementary Video 2 Evolution of the actin cytoskeleton from the radial into the chiral pattern. Images were recorded at 2 minute intervals over a period of ~ 4 hours. Display rate is 7 frames/sec and corresponds to the time-lapse series in Fig. 5 (untreated).

Supplementary Video 3 Organization of radial and transverse fibers seen in confocal microscopy Z-section. Cells were fixed and stained with phalloidin to visualize actin. Images of the actin structures at the cell edge of non-dehydrated cell on a circular island were captured by Z-stepping at 0.25 μm per step from the bottom to the top of the cell.

Supplementary Video 4 Electron tomographic reconstruction of intersection between transverse and radial fibers. Movie showing successive 2-nm slices of the tomographic reconstruction (10 frames/sec) as shown in Supplementary Fig. 2f. The image display starts from the top, goes to the bottom, and then back up to the top.

Supplementary Video S5 Movement of myosin V- or VI-coated nanoparticles (green) along filopodial cell projections (red) of fixed extracted cell. An asterisk (*) indicates a filopodium. Myosin V-coated nanoparticles moved towards filament barbed ends away from the cell body, while myosin VI-coated nanoparticles moved towards filament pointed ends in the direction of the cell body. Images were recorded at half a second intervals. Display rate is 30 frames/sec.

Supplementary Video 6 Movement of myosin V- (left) and myosin VI-coated (right) nanoparticles (green) along the actin transverse fiber (red) of fixed extracted cell. Note that the movements of both myosin V- and VI-coated nanoparticles could proceed in opposite directions along the same transverse fibers. Images were recorded at half a second intervals. Display rate is 7 frames/sec and corresponds to Fig. 3d-f (myosin V) and Supplementary Fig. 3b-e (myosin VI).

Supplementary Video 7 Actin dynamics upon treatment with the 10 μM formin inhibitor, SMIFH2. Images were recorded at 2 minute intervals over a period of ~ 3.5 hours. Display rate is 20 frames/sec and corresponds to the time-lapse series in Fig. 4a (lower panel).

Supplementary Video 8 Growth of radial fiber is dependent on formin activity. SMIFH2-treated cell was monitored for ~1 hour prior to drug washout. The recovery phase was followed for ~ 14 hours with images taken at 2 minute interval. Display rate is 30 frames/sec. Note the recovery of radial fibers growth started at ~ 3 hours after drug washout, at the cell periphery.

Supplementary Video 9 Actin dynamics upon treatment with 100 μM Y27632 (left) or 50 μM blebbistatin (Bleb, right). Images were recorded at 2 minute intervals over a period of ~ 5 hours. Display rate is 20 frames/sec and corresponds to the time-lapse series in Fig. 5.

Supplementary Video 10 Actin dynamics upon treatment with 1 μM nocodazole. Images were recorded at 2 minute intervals over a period of ~ 5 hours. Note that depolymerization of microtubules does not interfere with formation of chiral pattern and does not change handedness of the actin swirl. Display rate is 20 frames/sec and corresponds to the time-lapse series in Fig. 5.

Supplementary Video 11 Handedness of the chiral pattern in cell expressing low (left) or high (right) level of GFP-α-actinin-1. Radial fibers were visualized with GFP-α-actinin-1. Images were recorded at 2 minute intervals over a period of ~ 6 hours. Display rate is 20 frames/sec and corresponds to Fig. 6a.

Supplementary Video 12 A typical example of actin dynamics in cell expressing truncated mutant GFP-ABDdel-α-actinin-1. Images were recorded at 4 minute intervals over a period of ~ 9 hours. Display rate is 6 frames/sec and corresponds to the time-lapse series in Fig. 7a.

Supplementary Video 13 A typical example of actin dynamics in α-actinin-1 knockdown cell. Images were recorded at 3 minute intervals over a period of ~ 9 hours. Display rate is 8 frames/sec and corresponds to the time-lapse series in Fig. 7f.

Supplementary Video 14 Rotation of the microtubule array in the counter-clockwise direction, together with counter-clockwise swirling of the actin network, seen in cell expressing GFP-tubulin and tdTomato-F-Tractin to visualize microtubule and actin respectively. Images were recorded at 2 minute intervals over a period of ~ 12 hours. Display rate is 30 frames/sec.

Supplementary Video 15 Simulation of the chiral self-organization of the actin cytoskeleton. Corresponds to Fig. 8b.

Supplementary Video 16 Simulation showing polymerization of a free actin filament capped by formin-FH2 dimer. Actin monomers are shown in green (dark and light green are used to distinguish the long pitch helices). FH2 dimer is shown in blue-red. Note the rotation of the formin dimer.

Supplementary Video 17 Simulation showing polymerization of actin filament capped by an immobilized formin-FH2 dimer. Actin monomers are shown in green (dark and light green are used to distinguish the long pitch helices). FH2 dimer is shown in blue-red. Note the rotation of the actin filament.

Supplementary Video 18 Simulation showing polymerization of actin filament capped by an immobilized formin-FH2 dimer, and prevented from rotating at the pointed end. Actin monomers are shown in green (dark and light green are used to distinguish the long pitch helices). FH2 dimer is shown in blue-red. Immobilized monomers at the tip of the filament are shown in yellow. Note the periodic high amplitude rotation of the actin filament upon transit release of the contact of its barbed end with formin dimer ("screw-steps"; highlighted by change in background color from black to light gray).

Supplementary Note for

Cellular chirality arising from the self-organization of the actin cytoskeleton

Yee Han Tee, Tom Shemesh, Visalatchi Thiagarajan, Rizal Fajar Hariadi, Karen L. Anderson, Christopher Page, Niels Volkmann, Dorit Hanein, Sivaraj Sivaramakrishnan, Michael M. Kozlov, Alexander D. Bershadsky

COMPUTATIONAL MODEL

Computational procedure. Each discrete computational step contains the following transformations of the system:

1. A new TF is formed between each pair of mature FAs with a probability $r_{TSF}\,\Delta t$, where Δt is the time corresponding to one computational step and r_{TSF} is the rate of TF generation.

2. The internal stress within all the TFs including the newly generated ones is set to be equal $\gamma = \gamma^*$. The length L of each TF is then determined by the position of its endpoints bound to two RFs. The effective relaxed length L_0 of each TF, is set such that

    $$\frac{L-L_0}{L_0}\,k_s = \gamma^*.$$

3. The force on each TF endpoint, f_n, is calculated by taking the component of the internal stress γ^* parallel to the local direction of the RF to which it is bound.

4. The total force, F_m, acting on each RF is calculated as the sum of the forces applied by all the TFs that are bound along its length, $F_m = \sum_{n\ bound\ to\ m}(f_n)$.

5. The endpoints of each TF advance along the RFs to a distance $\Delta s = \beta f_n \Delta t$ meaning that the velocity of each endpoint is proportional to the force f_n applied to it, according to the linear friction law.

6. The new relaxed length L_0 of each TF is adjusted to the new distance between its ends such that the TF internal stress remains constant and equal γ^*.

7. The total elastic energy of the system is calculated as the sum of the stretching energies of all the TFs and of the bending energies of the RFs:

    $$\varepsilon_{tot} = \sum_{n \in TSF} \frac{(L-L_0)^2}{L_0}\frac{1}{2}k_s + \sum_{m \in RB} \int_{t=0}^{t=L_{RB}} k_{bend}\, c_m(t)^2 dt,$$

    where the integration in the second terms is performed along the RF length.

8. The change of configurations of all RFs is determined numerically by minimizing the total energy ε_{tot} with respect to the RF shapes.

9. Each FA is grown or disintegrated, depending on whether the force applied to it by the attached RFs exceeds or is lower than a threshold growth force, f^*, according to the model suggested in Shemesh et al.[1,2],

$$r_{FA} = \begin{vmatrix} r_{grow} & \Gamma(0) > f_{threshold} \\ 0 & \Gamma(0) = f_{threshold} \\ -r_{shrink} & \Gamma(0) < f_{threshold} \end{vmatrix}$$

10. A pair of RFs whose ends are connected by a TF, and are closer than a minimal distance Δ_{fuse}, are fused with a probability related to the angle between them, φ :

$$p_{fuse} = p_0 \, \Delta t \, e^{(\varphi - \pi)^2}$$

where p_0 is the rate of fusion attempts

Un-fused RFs are elongated by polymerization at a rate

$$r_{pol} = \begin{vmatrix} 0 & \Gamma(0) < \Gamma_{min} \\ a(\Gamma(0) - \Gamma_{min}) & \Gamma_{min} < \Gamma(0) < \Gamma_{max} \\ r_{max} & \Gamma(0) > \Gamma_{max} \end{vmatrix}$$

and contract locally at rate

$$r_{short}(s) = b \cdot (\Gamma(s) - \Gamma^*)$$

where a, b are fitting parameters in the model.

Detailed description of chiral asymmetry model. In the "rack and pinion" picture, rotation of individual filaments in RF about their axis (local direction $\hat{x}$, see Supplementary Figure 8) generates a frictional force on the TF in the local direction $\hat{y}$. Since RF are bound to TF at points $x > 0$, a torque develops about their anchoring to the FA at $x = 0$, corresponding to a CCW rotation pattern for $f_y < 0$; and a CW rotation pattern for $f_y > 0$.

A general friction mechanism coupling the rotation of the filaments to the TF may be expressed as

$$\vec{f}(t) = \beta \, (|\vec{\omega}(t) \times (a\hat{z})|)^{\alpha - 1} (\vec{\omega}(t) \times (a\hat{z})) \tag{1}$$

where a is the radius of the filament, β is a friction coefficient and α is the exponent describing the velocity dependence of the friction force.

Formin processive cappers continuously track the growing barbed ends of actin filaments. Due to the helical structure of the F-actin filaments, the orientation of formins relative to the bulk of the filaments must rotate with the addition of each new actin monomer. When not constrained, a formin capper tracks the right-handed long-pitch actin helix in a "stair-stepping" mode, so that addition of each new actin monomer results in $\sim -14°$ rotation of the formin about $\hat{x}$ (Supplementary Video 16). Conversely, if the formin dimer is immobilized while the pointed end of the filament is free to rotate, the bulk of the polymerizing actin filament will rotate along its axis in opposite direction (Supplementary Figure 8a and Supplementary Video 17). The angular velocity of a filament under such conditions is given by

$$\vec{\omega}_{ss} = \frac{14°}{\tau_{ss}} \, \hat{x} \tag{2}$$

where τ_{ss} is the time associated with a single stair-step motion of the formin. The frictional force exerted on the tSF, $\vec{f}_{free}$, is then

$$\vec{f}_{free} = -\beta (\omega_{ss} a)^\alpha \, \hat{y} \tag{3}$$

, thereby promoting CCW patterns.

We next consider a filament that, in addition to being capped by an immobilized formin, is prevented from rotating at its pointed end. Under these conditions, continuous polymerization of the filament results in accumulation of torsional strain in the bulk of the filament. Moreover, the zero-rotation constraint may be applied at any distance from the growing barbed end and not necessarily at the pointed tip, resulting in strain being accrued at the region between the formin and the non-rotating region. We propose that

cross-linking between actin filaments within a bundle can effectively prevent the rotation of the individual filaments.

A possible mechanism for relieving the torsional strain is suggested from the symmetry of the formin dimer. The configuration of the formin-actin complex after a stair-stepping polymerization step in which formin and actin rotate by 14° relative to each other is identical to that resulting from a polymerization step with a relative rotation of 166° in the opposite direction. We have previously suggested that employing such inverse rotations, termed "screw-steps" can limit the strain in the filaments (Supplementary Figure 8b and Supplementary Video 18). The optimal regime for processive capping under these constraints was found to consist of ~12 stair-steps followed by one screw-step[3]. In this regime, the rotation velocity of a bound filament alternates according to:

$$\vec{\omega}_{bound}(t) = \begin{bmatrix} \vec{\omega}_{ss} & 0 < t < 12\,\tau_{ss} \\ \vec{\omega}_{sc} & 12\,\tau_{ss} < t < \ 12\,\tau_{ss} + \ \tau_{sc} \end{bmatrix} \qquad (4)$$

where τ_{sc} is the time required for a single screw-step of formin, and $\vec{\omega}_{sc}$ is the angular velocity of the filament bulk during a screw-step, given by

$$\vec{\omega}_{sc} = -\frac{166°}{\tau_{sc}}\hat{x} \qquad (5)$$

The time average friction force produced by an actin filament under such conditions is given by:

$$\langle \vec{f}_{bound} \rangle = \int_{0}^{12\tau_{ss}+\tau_{sc}} \vec{f}_{bound}(t)\,dt \big/ (12\tau_{ss} + \tau_{sc}) \qquad (6)$$

Using (Eq. 1-5) in (Eq. 6), we get

$$\langle \vec{f}_{bound} \rangle = \frac{\beta a^{\alpha}\,[-(|\omega_{ss}|)^{\alpha}\cdot 12\tau_{ss}+(|\omega_{sc}|)^{\alpha}\cdot\tau_{sc}]}{12\tau_{ss}+\tau_{sc}}\,\hat{y} \qquad (7)$$

Assuming the time for each polymerization step to be constant, $\tau_{ss} = \tau_{sc}$, then for any $\alpha > 1$ we find that $\langle \vec{f}_{bound} \rangle > 0$. While, in fact, a stair-step may require less time than a screw-step due to energetic barriers to the latter, this has only a weak effect on the minimal force-velocity exponent. Moreover - while we treat here a specific mechanism for relaxation of the stresses within a bound, polymerizing filament, the friction force produced by such filaments is expected, in general, to promote CW swirl patterns in the system.

The fraction of the filaments in the RF that are immobilized by cross-linkers, λ, is expected to correspond to the expression levels of α-actinin. The mean force, $\vec{F}$, exerted on the TF in the system by all the rotating filaments is then given by:

$$\vec{F} = \lambda \langle \vec{f}_{bound} \rangle + (1 - \lambda)\langle \vec{f}_{free} \rangle \tag{8}$$

As expression level of α-actinin cross-linkers increases, this force changes sign, and the system transitions from favoring counter-clockwise to clockwise patterns.

REFERENCES

1. Shemesh, T., Verkhovsky, A.B., Svitkina, T.M., Bershadsky, A.D. & Kozlov, M.M. Role of focal adhesions and mechanical stresses in the formation and progression of the lamellipodium-lamellum interface [corrected]. *Biophysical journal* **97**, 1254-1264 (2009).
2. Shemesh, T., Bershadsky, A.D. & Kozlov, M.M. Physical model for self-organization of actin cytoskeleton and adhesion complexes at the cell front. *Biophysical journal* **102**, 1746-1756 (2012).
3. Shemesh, T., Otomo, T., Rosen, M.K., Bershadsky, A.D. & Kozlov, M.M. A novel mechanism of actin filament processive capping by formin: solution of the rotation paradox. *The Journal of cell biology* **170**, 889-893 (2005).